Check for updates

ADVANCED FUNCTIONAL MATERIALS
www.afm-journal.de

Implantable MicroLED-Mediated Chemo-Photodynamic Combination Therapy for Glioma Treatment

Jeongrae Kim, Hin Kiu Lee, Junwon Park, Seong Ik Jeon, Il Seong Lee, Wan Su Yun, Yujeong Moon, Jiwoong Choi, Man Kyu Shim, Jinseong Kim, Hanhee Cho, Nayeon Shim, Namcheol Hwang, Gyan Raj Koirala, Minjun Gwak, Sangheon Han, Dong-Hwee Kim, Won Seok Chang, Tae-il Kim,* and Kwangmeyung Kim**

Photodynamic therapy shows promise for glioma treatment with powerful efficacy and low resistance, however, its effectiveness is significantly lowered by inadequate light delivery through the skull. Herein, a needle-type implantable microLED device and cathepsin B-responsive prodrug nanoparticles (PNPs) are newly exploited for glioma's chemo-photodynamic combination therapy. The microLED containing four small LEDs on the tip of its guide needle can be implanted into the center of glioma tissues without large area opening of skull, uniformly irradiating light to deep glioma tissues. PNPs are formulated via self-assembly of heterobifunctional prodrug composed of doxorubicin, verteporfin, and cathepsin B-cleavable peptide linker, wherein they stably maintain inactive nanoparticle structures in normal physiological conditions and specifically deliver therapeutic age to cathepsin B-overexpressed glioma tissues. In vitro cellular assays, PNPs irradiated with showed the synergistic cytotoxicity of DOX and VFP only in cathepsin B-overexpressed cancer cells rather than normal cells. In tumor-bearing mice, PNPs showed high tumor accumulation via the nanoparticle-driven enhanced permeation and retention (EPR) effect and they also exhibited remarkable therapeutic efficacy against glioma under microLED-mediated light irradiation via chemo-photodynamic combination therapy. Accordingly, applying microLED with PNPs is an outstanding strategy to defeat glioma with cooperative chemo-photodynamic effects, minimal invasiveness, and desirable systemic/local safety.

1. Introduction

Glioma, the most common primary brain cancer, often presents complicated challenges in its treatment, indicated by high fatality rates with a bad prognosis and a short median life expectancy of 12 −18 months in its malignant form.[1] Despite decades of medical advancements, achieving its complete remission remains difficult due to prevalent recurrence, rapid proliferation, and aggressive metastasis.[2] Current therapeutic procedures for glioma mainly involve surgical resection, radiation therapy, and chemotherapy. A surgical resection is a major option for glioma treatment, however, it is often limited by infiltrative growth of tumors to deep parenchyma and causes a high risk of loss in essential brain integrity during the surgery.[3] Radiation therapy is an effective approach for primary glioma treatment, but it is highly lethal for normal brain tissues as well thereby hard to use for tumor-invasive regions.[4] Moreover, glioma exhibits low responsiveness to chemotherapy due to its strong resistance to anticancer drugs, necessitating the co-administration

J. Kim, I. S. Lee, W. S. Yun, Y. Moon, D.-H. Kim
KU-KIST Graduate School of Converging Science and Technology
Korea University
145 Anam-ro, Seongbuk-gu, Seoul 02841, Republic of Korea

The ORCID identification number(s) for the author(s) of this article can be found under https://doi.org/10.1002/adfm.202316386

© 2024 The Author(s). Advanced Functional Materials published by Wiley-VCH GmbH. This is an open access article under the terms of the Creative Commons Attribution-NonCommercial License, which permits use, distribution and reproduction in any medium, provided the original work is properly cited and is not used for commercial purposes.

DOI: 10.1002/adfm.202316386

H. K. Lee, G. R. Koirala, M. Gwak, T.-il Kim
School of Chemical Engineering
Sungkyunkwan University (SKKU)
2066 Seobu-ro, Jangan-gu, Suwon 16419, Republic of Korea
E-mail: taeilkim@skku.edu

J. Park, S. Han, W. S. Chang
Department of Neurosurgery and Brain Research Institute
College of Medicine
Yonsei University
50–1 Yonsei-Ro, Seodaemun-gu, Seoul 03722, Republic of Korea
E-mail: changws0716@yuhs.ac

16163028, 2024, 30, Downloaded from https://onlinelibrary.wiley.com/doi/10.1002/adfm.202316386 by Ewha Womans University Library, Wiley Online Library on [10/11/2024]. See the Terms and Conditions (https://onlinelibrary.wiley.com/terms-and-conditions) on Wiley Online Library for rules of use; OA articles are governed by the applicable Creative Commons License

of other agents to boost the chemotherapeutic efficacy. The complex heterogeneity and frequent mutation of glioma further impede the efficacy of single therapeutic modalities, highlighting the urgency for the combination of various therapeutic strategies to address the complex tumor microenvironment and improve patient outcomes.[5]

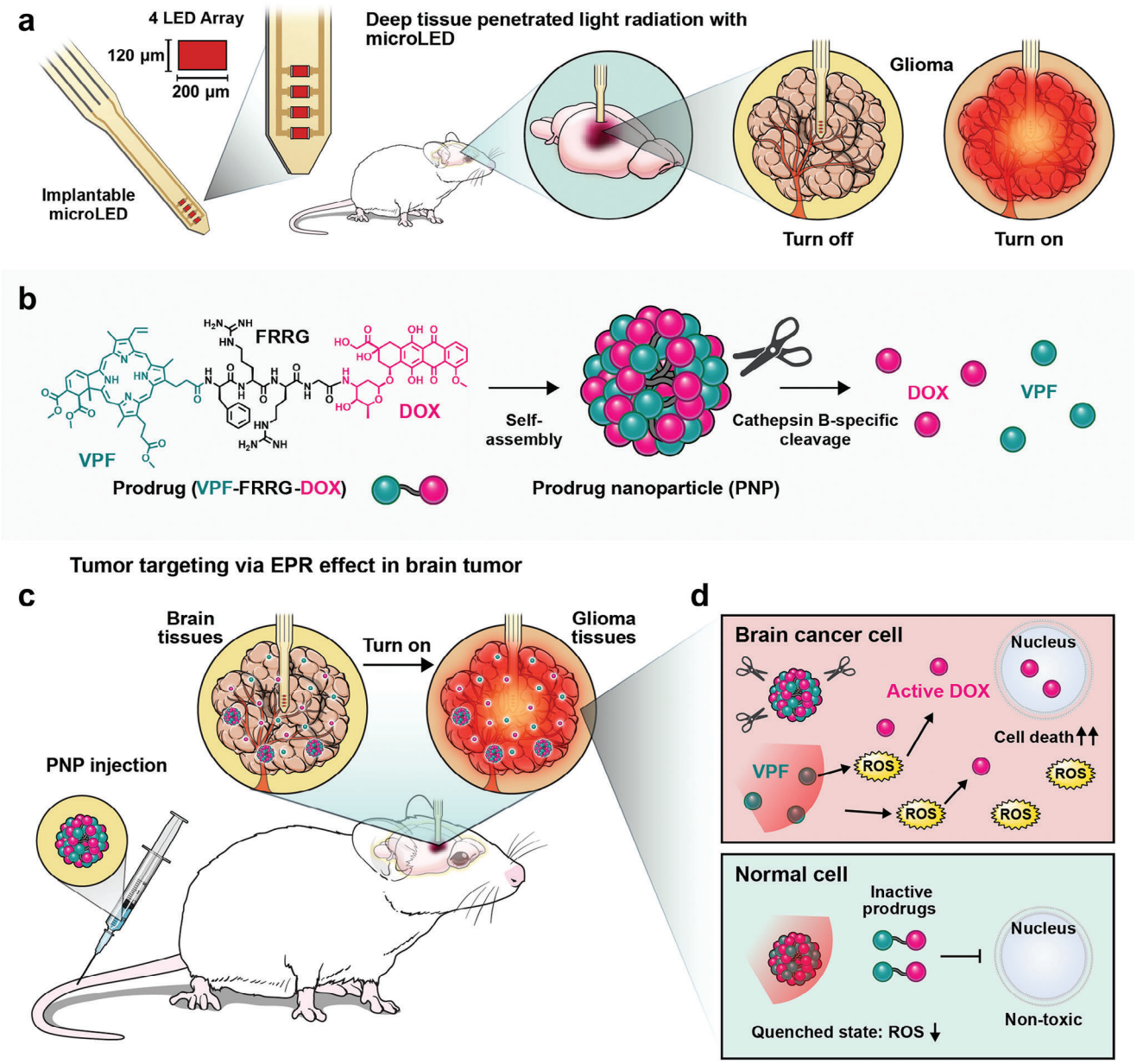
Photodynamic therapy (PDT) has emerged as a promising alternative for glioma treatment due to its loco-regional specificity and strong efficacy.[6] During PDT, photosensitizers delivered to tumor tissues are activated by light irradiation with certain wavelength ranges generating reactive oxygen species (ROS) that induce oxidative damage-associated cytotoxicity.[7] This PDT mechanism does not target a single cellular component, which helps effectively circumvent drug resistance in glioma tumors and endows strong therapeutic effects.[8] Moreover, photosensitizers are activated only at the site of light exposure, allowing a highly selective effect on glioma tissues while reducing the off-target damage to normal brain tissue.[9] Encouraged by the advantages of PDT in glioma treatment, the combination of PDT and other treatments such as surgical resection, chemotherapy, and radiation has demonstrated the potential to improve therapeutic outcomes.[10] Additionally, PDT can stimulate the programmed cell death of cancer cells, known as immunogenic cell death, which triggers the anticancer immune response and suppresses the recurrence and metastasis of glioma via systemic immune activation.[11] However, PDT efficacy would be significantly compromised by ensuring adequate light delivery to the deep tumor region.[12] Insufficient light delivery drastically diminishes the PDT efficacy in glioma, especially considering the obstruction by the skull, resulting in relapse and deadly progression.[13]

Due to the limitation of light delivery, light-emitting diode (LED) systems have played a pivotal role in medical and clinical advancements since their introduction in the 1900s.[14] However, when it comes to treating deep-seated tumors like glioma, traditional LED systems including bulky epoxy encapsulation have faced limitations due to their inability to penetrate through the skull and reach the tumor site effectively, such as organ damage and postoperative adhesion, thus limiting the biological application in PDT.[15] In contrast to conventional LED, a needle-type implantable microLED device was proposed as an intratumoral injectable light-irradiating device that offers compact size and site-specific PDT at targeted tumor tissues, overcoming the challenges of tumor depth with minimal invasiveness at a low cost.[16,17] Practically, this device consisted of a 5.5 mm guide needle and multiple arrayed red light-emitting LEDs on the tip of the needle for the tumor-specific PDT. The microLED could be inserted into the center of tumor tissues thereby the light was sufficiently irradiated to the deep tumor regions. The light intensity of microLED was freely controllable without its thermal degradation, thereby the effective photosensitizer activation and following cancer cell damage were consistently achieved not only at the irradiated site but also at the marginal tumor area. Furthermore, the moderate and site-specific PDT by microLED guidance efficiently promoted immunogenic cell death of tumor tissues without severe inflammation, resulting in complete tumor remission through the stimulation of antitumor immune responses upon the simultaneous administration of immune checkpoint inhibitors.[16] This study demonstrated the potency of implantable microLED as a deep-tissue light-delivering system to enhance the efficacy of PDT.

Herein, it was expected that our needle-type implantable microLED irradiation system would be highly advantageous for PDT of glioma since it can deliver light sources inside the skull. In addition, the combinatorial application of microLED-mediated PDT and chemotherapy is considered to exhibit great potency in glioma treatment since not only do they elicit their respective therapeutic effects, but PDT further boosts the chemotherapy by assisting it in overcoming the harsh tumor heterogeneity and drug resistance of glioma as well.[18] Therefore, a new approach of implantable needle-type microLED-guided chemophotodynamic combination therapy cooperatively using the implantable microLED and chemodrug-photosensitizer dual prodrug nanoparticles (PNPs) which is mainly responsive to brain cancer cell-overexpressed cathepsin B was suggested for glioma treatment. The needle-type implantable microLED is constructed by placing four LED devices on the edge of biocompatible polymeric guide needles, wherein the LEDs are allowed to emit lights with a precisely controlled intensity at the exact site of application (**Scheme 1a**). The guide needle is designed to be thin but tough enough so that the microLED can be inserted directly into glioma tissues in a minimally invasive manner, without a wide surgical opening of the skull. The cathepsin B-responsive PNPs are fabricated via the self-assembly of heterobifunctional prodrug, named VPF-FRRG-DOX, which are the chemically conjugated molecules containing doxorubicin (DOX), photosensitizer (verteporfin, VPF), and cathepsin B-cleavable peptide (*Phe-Arg-Arg-Gly*; FRRG) between them (Scheme 1b). Importantly, PNPs can be formed into stable nanoparticles in physiological conditions due to their amphiphilic molecular characteristics and intermolecular π–π interactions of DOX, FRRG, and VPF, facilitating their specific accumulation inside glioma tissues with tumoral angiogenic vessels via the enhanced permeability and retention (EPR) effect when intravenously administered (Scheme 1c).[19] Both DOX and VPF in PNPs maintain their inactivity before they are delivered to tumor tissues due to their cathepsin B-specificity. After reaching brain cancer cells, tumor-endocytosed PNPs are supposed to be degraded into VPF and free DOX in response to the cathepsin B enzymes, both VPF and DOX will synergistically eradicate tumor tissues via both ROS generation and DNA intercalation (Scheme 1d). The needle-type implantable microLED can effectively activate the ROS generation of VPF throughout entire tumor tissues via uniform light irradiation, and going further, the widespread ROS additionally increases the efficacy of DOX by aggravating tumor tissues to be vulnerable to DOX treatment.[20] Moreover, the

S. I. Jeon, J. Kim, H. Cho, N. Shim, K. Kim
College of Pharmacy, Graduate School of Pharmaceutical Sciences
Ewha Woman's University
52 Ewhayeodae-gil, Seodaemun-gu, Seoul 03760, Republic of Korea
E-mail: kimkm@ewha.ac.kr
J. Choi, M. K. Shim
Biomedical Research Institute
Korea Institute of Science and Technology (KIST)
5, Hwarang-ro 14-gil, Seongbuk-gu, Seoul 02792, Republic of Korea
N. Hwang
Department of Chemical and Biomolecular Engineering
Sogang University
35 Baekbeom-ro, Mapo-gu, Seoul 04107, Republic of Korea

 © 2024 The Author(s). Advanced Functional Materials published by Wiley-VCH GmbH



Scheme 1. Schematic illustration explaining the microLED-mediated chemo-photodynamic therapy of glioma with cancer-specific prodrug nanoparticles. a) Needle-shaped minimally invasive implantable microLED was produced by arraying four LEDs on the tip of the guide needle, which facilitates to control of the intensity of light irradiated to the deep tissues by the microLED. The microLED can directly and uniformly irradiate lights into the center of brain tumor tissues through the skull without opening surgery. b) Brain tumor-overexpressed cathepsin B-cleavable prodrugs (VPF-FRRG-DOXs) for microLED-mediated chemo-photodynamic therapy were synthesized via conjugating VPF and DOX to the *N*- and *C*-terminals of cathepsin B-cleavable FRRG peptide, respectively. The synthesized prodrugs are self-assembled into nanoparticles to form PNPs in aqueous media, then after being delivered to cathepsin B-overexpressed brain cancer cells, they are specifically cleaved to release DOX and VPF, eliciting combined chemo-photodynamic effect. c) Intravenously administered PNPs are supposed to be specifically accumulated inside glioma tissues by the EPR effect while preventing the undesirable delivery to normal organs including brain tissues. MicroLED would be implanted in brain tumor tissues through a pinhole in the skull, irradiating lights for PDT to the center of brain tumor tissues. d) PNPs stay in their dormant state before being cleaved by cathepsin B and are activated to release free DOX and VPF inside the cathepsin B-overexpressed brain tumor tissues. Accompanied by the microLED-mediated light irradiation inside the tumor, the released VPF and DOX exhibited strong therapeutic effects via DNA intercalation and ROS generation, respectively. Moreover, the broadly generated ROS throughout the tumor tissues by the activity of microLED and VPF would enhance the efficacy of DOX by suppressing the drug resistance of brain tumor tissues, resulting in synergistic chemo-photodynamic effects. In contrast, PNPs would show significantly reduced toxicity to normal cells since both DOX and VPF in PNPs keep their quenched state inside normal cells with low cathepsin B levels.

© 2024 The Author(s). Advanced Functional Materials published by Wiley-VCH GmbH

16163028, 2024, 30, Downloaded from https://onlinelibrary.wiley.com/doi/10.1002/adfm.202316386 by Ewha Womans University Library, Wiley Online Library on [10/11/2024]. See the Terms and Conditions (https://onlinelibrary.wiley.com/terms-and-conditions) on Wiley Online Library for rules of use; OA articles are governed by the applicable Creative Commons License

implantable microLED-guided localized light irradiation and tumor-specifically activatable PNPs will greatly mitigate the side effects in normal tissues. To validate our thesis, the implantable microLED and cathepsin B-responsive PNPs were prepared and their properties were first examined in vitro. After assessing the in vitro cellular uptake and cytotoxicity of PNPs, the biodistribution and tumor accumulation of intravenously administered PNPs in tumor xenografted mice were determined. Finally, the therapeutic efficacy and systemic toxicity of PNPs with needle-type microLED implantation were also investigated against in vivo subcutaneous brain tumor mouse and orthotopic glioma rat models.

2. Results and Discussion

2.1. Characterization of Implantable MicroLED

A needle-type implantable microLED device, designed for site-specific light irradiation of deep brain tumor tissues, was manufactured through photolithography techniques and subsequently employed for the PDT of glioma.[16,17] This microLED device featured a composite structure, consisting of an epoxy-based guide needle, an electrical insulating polyimide (PI) film, gold electrodes, four microLED arrays, and an epoxy waterproof coating, all sequentially laminated (**Figure 1a**). Briefly, the microLED fabrication process involved the assembly of gold electrodes and four red-light LED (120 × 200 μm) arrays onto a 5 μm-thick PI film (Scheme S1, Supporting Information). This assembly was then placed onto a 100 μm-thick polyacrylic acid (PAA) injection guide needle, finally followed by a coating with a 2 μm-thick transparent epoxy resin layer to glue them together. Each component layer of the microLED device exhibited sufficient flexibility and durability, ensuring resistance to fracture during its application. Moreover, these layers were securely bonded together using a PSA precursor, thereby preventing delamination. The visual inspection of the implantable microLED device was carried out utilizing various instruments, including a digital camera, a field emission-scanning electron microscope (FESEM), and an optical microscope (Leica DM2700M, Leica Microsystems Inc.) (Figure 1b). The dimensions of the device measured 10.0 × 2.25 × 0.15 mm (height × width × thickness). At the tip of the needle, four red microLEDs were integrated, each measured as 120 × 200 × 20 μm. The microLED was affixed to a 15 cm-long flat wire, facilitating a connection to a controllable power supply. Upon establishing the connection, it promptly emitted a vivid red light from the needle's tip. Importantly, the microLED's structural composition possessed the requisite attributes of flexibility and resilience, allowing it to endure moderate bending during its operational use without compromising its light emission (Figure 1c). After the fabrication process, the electrical and optical characteristics of the microLED were characterized using precision Source/Measure Unit (SMU) (B2901A, Agilent Technologies Inc.) and light spectrometry (HR4000, Ocean Optics Inc.) respectively. Figure 1d shows the relations between the applied voltage with both current (I-V curve) and output power. The microLED displayed a turn-on voltage of ≈1.8 V, beyond which the current exhibited a linear increase in proportion to the applied voltage. Correspondingly, the applied power demonstrated a gradual rise, commensurate with the input voltage exceeding 1.8 V. At 4 V of operation, the input power was measured at ≈35 mW, and this increased to 50 mW with a 4.5 V voltage application. Light output measurement from both the front and back sides of the microLED affirmed their adequacy for deep brain tumor PDT within deep brain tumor tissues. Of note, both the front and back sides exhibited a consistent turn-on voltage at ≈1.8 V (Figure 1e). The front side apparently delivered higher output power than the back side (see Figure 1e inset), ensuring precise directional light emission control. Four front LEDs efficiently delivered high-intensity light without significant efficiency loss, peaking ≈4 V and declining thereafter, establishing an optimal operational range for maximum light output. These insights are pivotal for precise light delivery applications. MicroLEDs were subsequently applied to various media and operated at different input power levels to assess their practical utility. In ambient conditions, the light intensity was dynamically controlled in response to input power, a critical factor in microLED-mediated photodynamic therapy to optimize therapeutic efficacy (Figure 1f). This controllability of light intensity remained consistent across various media, including air, water, in vivo tissues, and ex vivo brain tumor spheroid tissues. Notably, the microLEDs functioned reliably without experiencing flooding or electrical shorts, contributed by the presence of a PI film and epoxy coating (Figure 1g). Furthermore, the microLEDs could be directly implanted within tissues without operating open surgery, delivering light while remaining unaffected by biological components (Figure 1h). This direct implantation beneath the skin was made feasible through the use of a robust 5.5 mm probe in the form of a guide needle. The device's in vivo stability was ensured through the use of biocompatible materials, wherein the safety of microLED-composing materials has been fully demonstrated previously.[21] Importantly, the light emitted by the implanted microLEDs was harmless, causing neither skin burns nor irritation. To assess the extent of light penetration from the microLEDs' center to the periphery, microLEDs were implanted into ex vivo brain tumor spheroids and operated at various input power levels (Figure 1i). It was observed that the light was broadly distributed to the marginal region with an input power exceeding 50 mW. Thus, an input power of 50 mW was selected for the photodynamic therapy procedure.

To simulate the in vivo environment, we conducted a long-term operation measurement in both air and water settings. The device was activated in a specific pattern (1 min OFF, 5 min ON, and 1 min OFF), and the temperature levels were monitored using an infrared camera with the microLED continuously turned on. In the air environment, the device exhibited a substantial temperature increase, with an average temperature rise to ≈45 °C and occasional peaks nearing 80 °C from room temperature (Figure 1j). In contrast, the temperature showed a much smaller increase, with an average rise of ≈1 °C, compared to the OFF-state temperature (Figure 1k). These findings have critical implications for ensuring the safety of biological subjects during the long-term application of microLED to the brain, particularly concerning potential thermal damage to tissues and cells. The low heat generation of microLED is also advantageous for mediating photodynamic therapy, as excessive heat could weaken the therapeutic outcomes.[22] During monitoring, the microLED's electrical operation remained consistently active in air, in in vivo normal brain, and in ex vivo brain tumor spheroid media for a continuous 1.5-h period (Figure 1l). This implantable microLED device

© 2024 The Author(s). Advanced Functional Materials published by Wiley-VCH GmbH

16163028, 2024, 30, Downloaded from https://onlinelibrary.wiley.com/doi/10.1002/adfm.202316386 by Ewha Womans University Library, Wiley Online Library on [10/11/2024]. See the Terms and Conditions (https://onlinelibrary.wiley.com/terms-and-conditions) on Wiley Online Library for rules of use; OA articles are governed by the applicable Creative Commons License

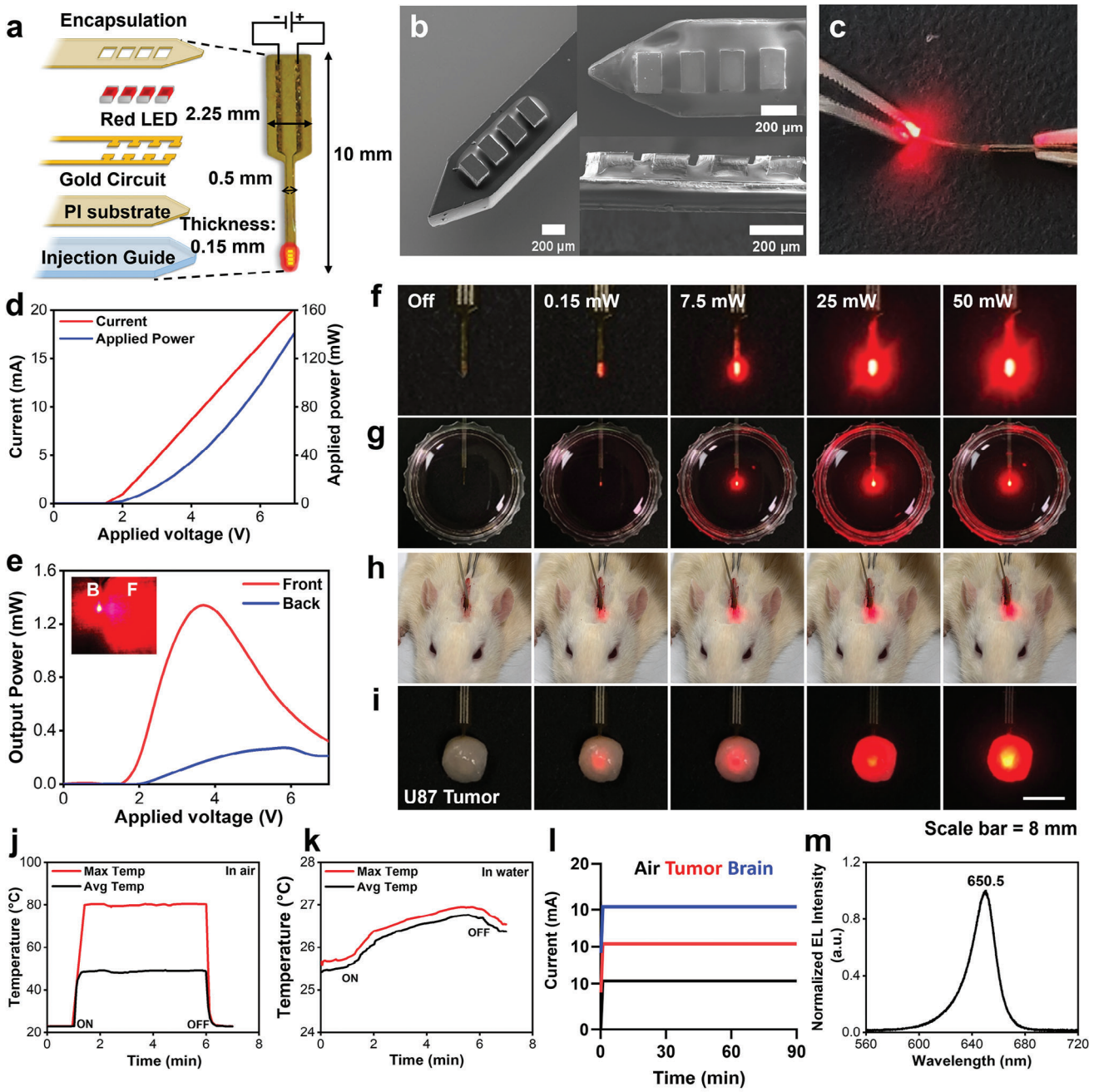


Figure 1. Characterization of microLED. a) A digital image and graphical illustration showing the specific structure and composition of microLED. b) Magnified SEM images of microLEDs on a needle tip, showing their side and top structures. c) Digital images of microLED after its connection to the power supply, moderately bent using forceps. d) The electrical property of microLED depending on the applied voltage and power. e) The output power of microLED depending on the applied voltage, measured both at the front and back sides of the device. Digital images showing the intensity of light from microLED with different input powers in f) the air condition, g) the aqueous condition, h) the actual tissue, and i) the tumor spheroids. The maximum and average temperatures changes in j) air and k) water media after the application of microLED and during its operation. l) The current changes of microLED in aqueous media, brain, and tumor tissues during its 1.5 h-operation. m) The wavelength of light emitted from the microLED.

could be successfully inserted into brain or brain tumor tissues, enabling localized light irradiation for over 1.5 h while maintaining a power intensity of 50 mW, contributed to its protective encapsulation and thermal diffusion to the surroundings. Through comprehensive assessments of its electrical characteristics, tissue compatibility, light delivery within deep tissues, and long-term durability, we confirmed that the microLED device may demonstrate the necessary operational qualities for its potential applications in photodynamic therapy.

The selection of wavelength is also a critical factor in PDT. In our study, the emitted light exhibited a wavelength of 645 nm, attributable to the use of red light LEDs (Figure 1m). This precise

© 2024 The Author(s). Advanced Functional Materials published by Wiley-VCH GmbH

16163028, 2024, 30, Downloaded from https://onlinelibrary.wiley.com/doi/10.1002/adfm.202316386 by Ewha Womans University Library, Wiley Online Library on [10/11/2024]. See the Terms and Conditions (https://onlinelibrary.wiley.com/terms-and-conditions) on Wiley Online Library for rules of use; OA articles are governed by the applicable Creative Commons License

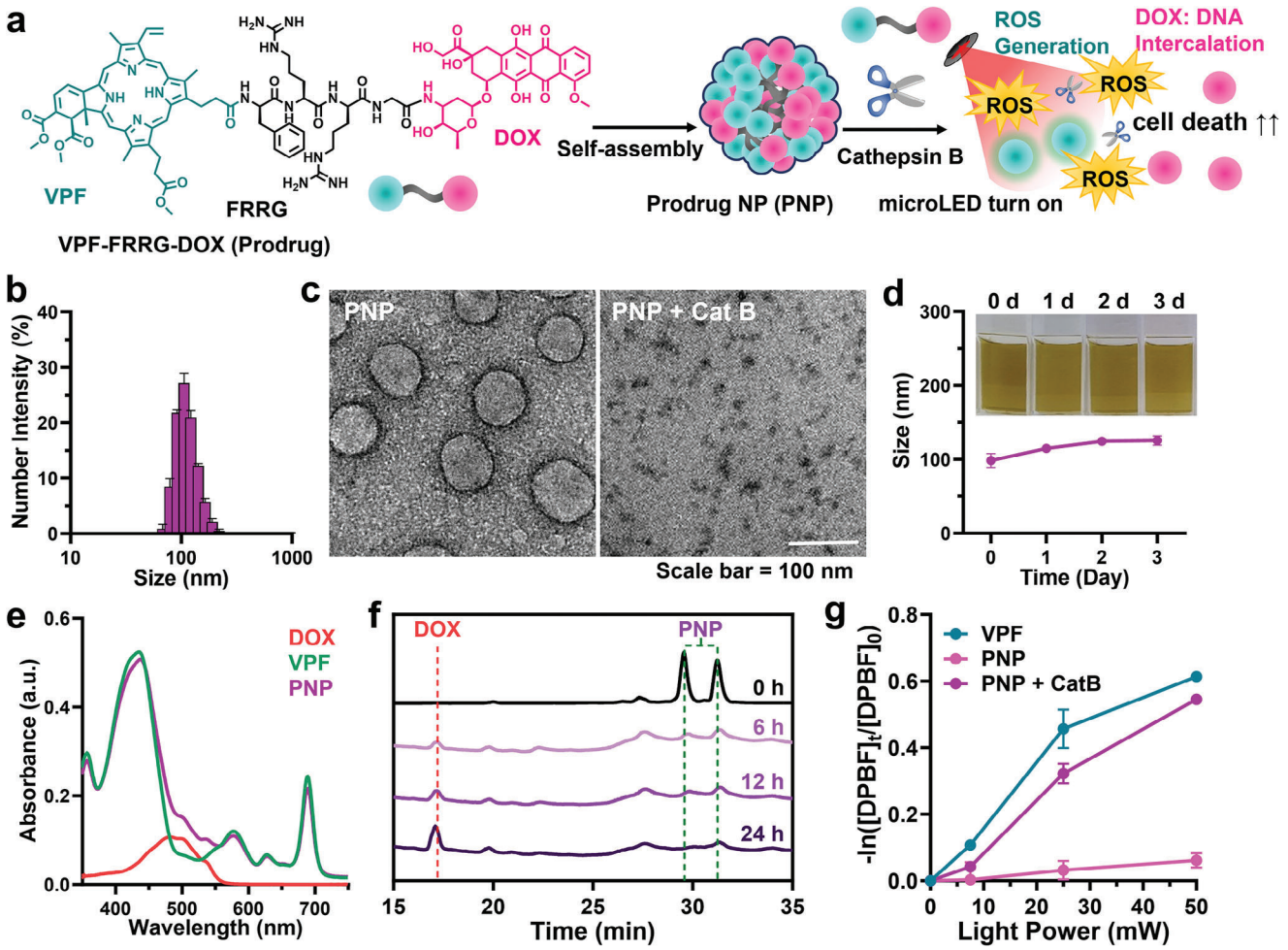


Figure 2. Characterization of PNPs. a) A graphical Scheme showing the specific chemical structure of VPF-FRRG-DOX prodrug and the mode of action of PNPs. VPF-FRRG-DOX prodrugs spontaneously form nanoparticles themselves in aqueous media and are specifically activated by cathepsin B to release DOX and VPF. The released DOX kills cancer cells by DNA intercalation, and the VPF generates ROS under light irradiation. b) The DLS data of PNPs (1 mg/mL) showing their hydrodynamic diameter. c) A TEM image of PNPs (1 mg mL^{-1}) displaying their spherical and rigid morphology before the cathepsin B treatment and their dissociation after 24 h-treatment of cathepsin B (0.1 μg mL^{-1}). d) The 3-day dispersion stability of PNPs in PBS (1 mg mL^{-1}), analyzed via DLS. e) UV-vis absorption spectra of free DOXs, free VPFs, and PNPs at the same concentrations (1 mM). f) Time-dependent changes in the HPLC spectra of PNPs (1 mg mL^{-1}) under the presence of 0.1 μg mL^{-1} cathepsin B, due to their cathepsin B-specific cleavage. g) The ROS generation of VPFs, PNPs, and PNPs with cathepsin B under light irradiation with increasing power input, indicated by the DPBF probe.

wavelength selection is crucial in optimizing tissue penetration and enhancing the activation of photosensitizing fluorophores (VPFs). This strategic choice effectively mitigates the potential risks to surrounding tissues, ensuring a focused and efficacious approach, particularly in the context of biological experiments and photodynamic therapy.

2.2. Characterization of Prodrug (VPF-FRRG-DOX) Nanoparticles (PNPs)

To achieve the brain cancer cell-specific chemo-photodynamic combination therapy, the prodrug of VPF-FRRG-DOX was synthesized by conjugating photosensitizer (verteporfin, VPF) and doxorubicin (DOX) to the *N*- and *C*-terminals of cathepsin B-cleavable FRRG peptide via the two-step amidation chemistry, respectively.[23] Due to its amphiphilic molecular structure and intermolecular π–π interactions of DOX, FRRG, and VPF, VPF-FRRG-DOX prodrug is supposed to spontaneously assemble into prodrug nanoparticles (PNPs) in an aqueous solution, and both DOX and VPF in PNPs maintain their inactive state before being cleaved by brain cancer cell-overexpressed cathepsin B (**Figure 2**a). Once PNPs are cleaved into free DOX and VPF under the presence of cathepsin B, they exhibit a strong antitumor effect through the DNA intercalation of DOX and ROS generation of light-irradiated VPF. The synthesized chemical structure of VPF-FRRG-DOX was confirmed by high-performance liquid chromatography (HPLC) and liquid chromatography-mass spectrometry (LC/MS) (Figure S1, Supporting Information). In the HPLC spectra, two sharp peaks appeared at 29.8 and 31.5 min due to the isomerization of VPF in the prodrug.[24] The LC/MS spectra of the prodrug exhibited a single peak and the measured molar mass was well matched to the theoretical value (m/z = 881.2, $[M + 2H^+]/2$). When prodrugs were dispersed in

© 2024 The Author(s). Advanced Functional Materials published by Wiley-VCH GmbH

16163028, 2024, 30, Downloaded from https://onlinelibrary.wiley.com/doi/10.1002/adfm.202316386 by Ewha Womans University Library, Wiley Online Library on [10/11/2024]. See the Terms and Conditions (https://onlinelibrary.wiley.com/terms-and-conditions) on Wiley Online Library for rules of use; OA articles are governed by the applicable Creative Commons License

PBS at a 1 mg mL^{-1} concentration, they were self-assembled into monodisperse nanoparticles with sizes of 98.32 ± 9.63 nm, resulting in PNPs (Figure 2b). Their morphology was further observed via transmission electron microscopy (TEM), demonstrating their rigid spherical structures and uniform nanometer sizes (Figure 2c). Once treated with cathepsin B, the PNPs lost their spherical shape due to the cleavage of FRRG peptide linkers and following particle dissociation. The size of PNPs in PBS was stably secured to 100 – 125 nm without notable aggregation or fragmentation (Figure 2d). The UV-Vis absorbance of the PNP solution was analyzed and compared to those of free VPF and DOX solutions at the same molar concentrations, wherein the spectra of PNPs were similar to those of VPF (Figure 2e). A small shoulder around 480 nm was additionally shown in their absorption spectra, which was consistent with the peak of free DOX. Subsequently, 0.1 mM PNPs were co-incubated with 10 μg mL^{-1} cathepsin B, and the changes in their HPLC peaks were assessed in a time-dependent manner. As the incubation time elapsed, the peak of PNPs rapidly decreased within 6 h post-incubation, and the peak corresponding to free DOX newly emerged (Figure 2f). After 24 h post-incubation with cathepsin B, 94% of PNPs were cleaved to release G-DOX and VPF, further proven via the LC/MS analysis (m/z = 623, [M + Na+]) (Figure S2, Supporting Information). The cleaved G-DOX was further degraded to free DOX by lysosomal enzymes in cathepsin B-overexpressed cancer cells.[25] Moreover, the ROS-generating ability of PNPs depending on the cathepsin B treatment was evaluated using the ROS-sensitive 1,3-diphenylisobensofuran (DPBF) fluorescent probe. Notably, PNPs before their cathepsin B-catalyzed cleavage did not generate ROS even with light irradiation since the excited VPF molecules would dissipate their energy to the adjacent VPFs when they are closely aggregated such as in nanoparticle forms, called the self-quenching effect of VPFs (Figure 2g).[23,26] In contrast, PNPs incubated with cathepsin B for 24 h exhibited ROS generation properties similar to free VPF solution, demonstrating the release of VPFs in the presence of cathepsin B. Therefore, the synthetic outcome, spontaneous nanoparticle formation, and cathepsin B-specific cleavage of PNPs were fully determined through a series of bench experiments.

2.3. In Vitro ROS Generation and Cytotoxicity of PNPs with Light Irradiation via MicroLED

Before assessing the cytotoxicity of PNPs with light irradiation, their endocytosis and intracellular distribution behaviors were investigated against human brain glioblastoma (U87), rat brain glioma (C6), and normal rat heart myoblast (H9C2) cells. In the western blot assay, U87 and C6 cancer cells expressed 6.1–6.5 fold higher cathepsin B levels than H9C2 normal cells, which would differentiate the intracellular distribution and toxicity of PNPs inside normal and brain cancer cells (**** $p < 0.0001$) (**Figure 3a**). 5×10^4 U87, C6, and H9C2 cells were separately cultured and treated with 1 μM DOX, VPF, and PNPs to compare their localization in cytosols and nuclei. When the cells were observed via confocal laser scanning microscope (CLSM) 24 h after treatment, DOX (red color) was mainly placed inside the nuclei regardless of cell type (Figure S3, Supporting Information). On the contrary, VPF (green color) was rarely detectable in nuclei of all cells and located in their cytosols since VPF could not penetrate the nuclear membrane (Figure S4, Supporting Information). In particular, PNPs exhibited different subcellular localization behaviors in normal and brain cancer cells. In the case of brain cancer cells, PNPs were cleaved into free DOX and VPF by cathepsin B inside the U87 and C6 cancer cells, then DOX and VPF were individually localized in nuclei and cytosols, respectively (Figure 3b). As a control, PNPs were not cleaved to release free DOX or transported to nuclei inside the H9C2 cells due to the low cathepsin B expression level of normal cells. The amounts of free DOXs located in nuclei of PNP-treated U87 and C6 cells were measured to be ≈69%, due to the cathepsin B-specific cleavage of PNPs in cancer cells (Figure 3c). However, 88% of DOX remained inside the cytosol of H9C2 cells at an uncleaved PNP state. This is deduced that PNP could not enter through the nuclear membrane before its cathepsin B-mediated cleavage due to its high molecular weight and bulky particle structure, whereas DOX freely and immediately reached cell nuclei with high diffusivity.[27] The intranuclear levels of DOX in U87 and C6 were 5.7 – 6.2-fold higher than that in H9C2, confirming the cathepsin B specificity of PNPs in subcellular levels (**** $p < 0.0001$). In the case of free DOX-treated cancer cells, 85 – 93% of free DOX was located inside the nuclei of U87 and C6 cells 24 h after its incubation, while only 69 – 81% of DOX was delivered intranuclearly with 24 h PNP treatment. This is because it took moderate time for PNPs to be cleaved by cathepsin B and release free DOXs after being taken up by cancer cells.

After determining the cellular uptake and cancer cell-specific intranuclear DOX delivery properties of PNPs, their photosensitization and ROS-generating properties under microLED-mediated light irradiation were evaluated against brain cancer cells. 5×10^4 U87 and C6 cells were cultured in 5 cm culture dishes, treated with 1 μM DOX, VPF, and PNPs for 24 h, and irradiated with red light (λ = 640 nm, 50 mW) for 15 min using microLED with a light intensity of 50 mV. Observing the in vitro ROS generation and the consequent apoptosis of cancer cells, bright ROS signals (DCFH-DA; green color) were visible only in VPF with microLED-mediated light (VPF^{+LED})- or PNPs with microLED-mediated light ($PNPs^{+LED}$)-treated ones (Figure 3d). The treatment of free DOX moderately induced the apoptosis (Annexin V; red fluorescence) of both U87 and C6 cells without ROS generation, which was also found in PNP-treated ones without light irradiation as DOXs released from PNPs by cathepsin B cleavage exhibited cancer cell-specific toxicity. As a control, VPF induced neither ROS generation nor cancer cell apoptosis in the dark condition. The light from microLED was broadly irradiated throughout the culture dishes thereby ROS was generated over a wide area (Figure 3e). The ROS generation areas of VPF^{+LED} and PNP^{+LED} treatment showed no significant difference from each other since they were dependent on the light-irradiated areas by microLED, not on the type of treated therapeutic agents. The treatment of DOX and VPF without light exhibited far-restricted ROS generation areas as they could not generate ROS. The apoptotic areas of DOX, PNP without light, and PNP^{+LED} treatment were similar to one another due to the apoptosis-inducing effect of DOXs. The intensities of ROS signals were measured to be 3.0 – 4.2-fold higher in VPF^{+LED}- and PNP^{+LED}-treated cells compared to the control or those with other treatments (Figure 3f). When quantifying the intensity of apoptotic fluorescence by

© 2024 The Author(s). Advanced Functional Materials published by Wiley-VCH GmbH

16163028, 2024, 30, Downloaded from https://onlinelibrary.wiley.com/doi/10.1002/adfm.202316386 by Ewha Womans University Library, Wiley Online Library on [10/11/2024]. See the Terms and Conditions (https://onlinelibrary.wiley.com/terms-and-conditions) on Wiley Online Library for rules of use; OA articles are governed by the applicable Creative Commons License

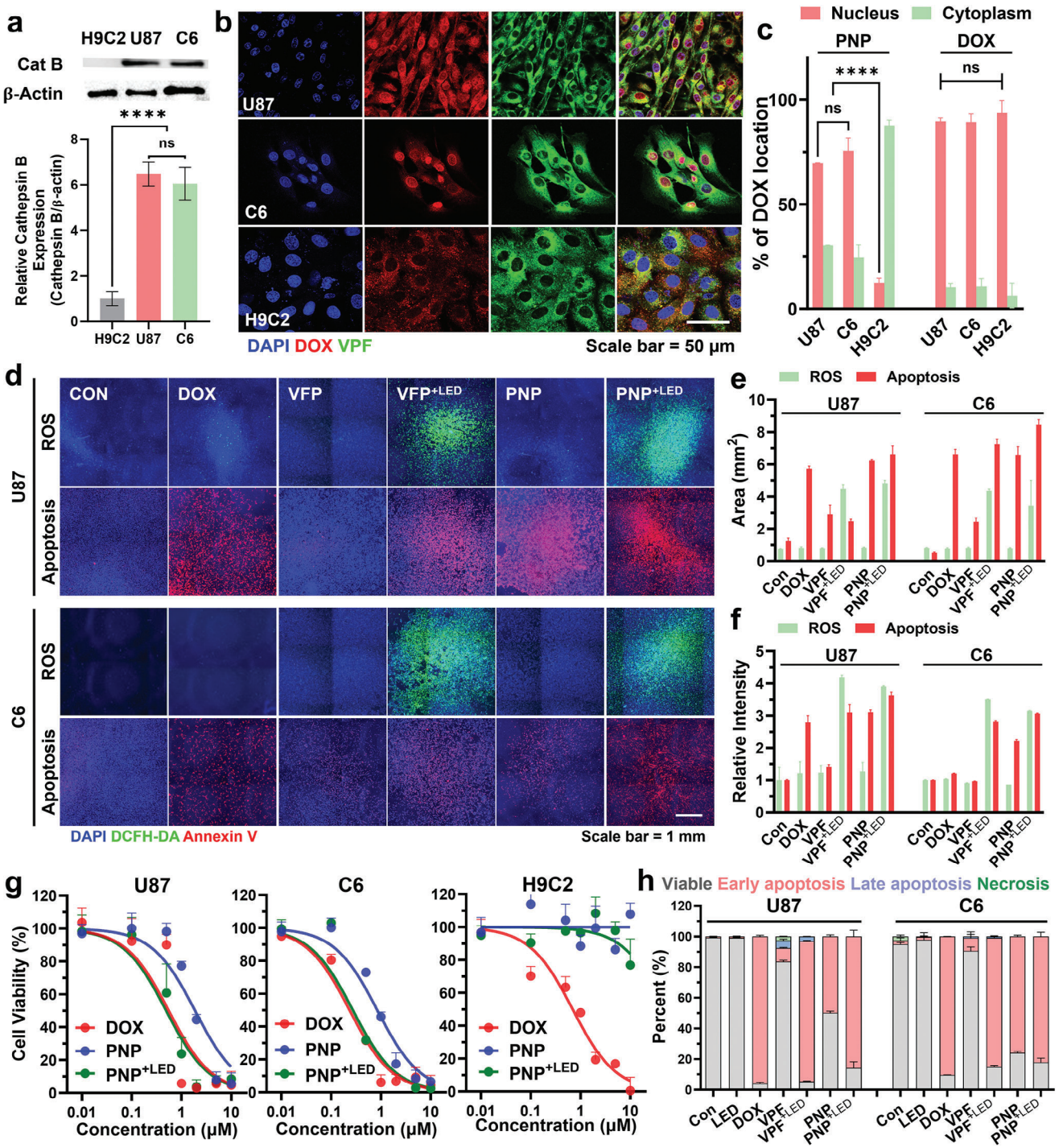


Figure 3. In vitro cellular uptake and cytotoxicity of PNPs. a) Western blot assay of U87 and H9C2 cells to compare their cathepsin B expression levels ($n = 3$). b) CLSM images of H9C2, U87, and C6 cells 24 h after their incubation with PNPs (1 μM), showing their endocytosis and intracellular distribution. c) The localization ratios of DOX fluorescent signals by DOXs or PNPs (1 μM, respectively) inside the cytosols or nuclei of H9C2, U87, and C6 cells 24 h post-treatment ($n = 3$). d) The in vitro ROS generation and apoptosis induction of DOXs, VPFs, and PNPs (1 μM, respectively) against U87 and C6 cells with or without light irradiation by microLED, and their quantitative analysis exhibiting e) the ROS-generated and apoptotic areas and f) relative fluorescent intensities by ROS generation and apoptosis. g) The viability of H9C2, U87, and C6 cells after the treatment with different concentrations (0.01 – 10 μM) of DOX, PNPs, and PNPs^{+LED}. h) Death patterns of U87 and C6 cells after the treatment of DOX, VPF without light, VPF^{+LED}, PNPs without light, and PNPs^{+LED} (1 μM, respectively), determined via PI and Annexin V staining. ns = not significant, **** $p < 0.0001$.

© 2024 The Author(s). Advanced Functional Materials published by Wiley-VCH GmbH

16163028, 2024, 30, Downloaded from https://onlinelibrary.wiley.com/doi/10.1002/adfm.202316386 by Ewha Womans University Library, Wiley Online Library on [10/11/2024]. See the Terms and Conditions (https://onlinelibrary.wiley.com/terms-and-conditions) on Wiley Online Library for rules of use; OA articles are governed by the applicable Creative Commons License

Annexin V, both U87 and C6 cells treated with PNPs^{+LED} expressed the highest signals due to the combined effect of DOX and VPF.

To assess the cancer cell-specific cytotoxicity of PNPs, 5×10^4 brain cancer and normal cells were incubated with various concentrations of DOX, VPF, and PNPs ranging from 0.01 to 10 μM for 24 h, followed by microLED-mediated light (50 mW) irradiation for 15 min. Their CCK-8 assay showed that PNPs effectively killed both U87 and C6 cells and their cytotoxicity became higher with the light irradiation (Figure 3g; Figure S5, Supporting Information). The IC_{50} values of PNPs in dark conditions against U87 and C6 cells were calculated as 1.88 and 0.84 μM, respectively, which were 1.4 – 4.2-fold higher than those of free DOX (0.46 (U87) and 0.23 (C6) μM) or VPF^{+LED} (0.45 (U87) and 0.62 (C6) μM) due to the delayed activation of PNPs and low intranuclear localization of DOXs as demonstrated above. However, the IC_{50} values of PNPs^{+LED} were lowered to 0.49 and 0.27 μM by the light irradiation, respectively, which was similar to those of DOX or VPF^{+LED}. The enhanced cytotoxicity of PNPs^{+LED} was contributed by the dual activation of free DOX and VPF in the cell culture system. On the contrary, PNPs elicited significantly reduced toxicity against normal H9C2 cells, wherein their IC_{50} value without light was not measurable. Their toxicity was slightly increased with light irradiation, resulting in their IC_{50} value of 51.45 μM, but still 38.4 – 74.2-fold higher than free DOX or VPF. It was considered that PNPs^{+LED} before their cathepsin B-catalyzed cleavage brought about their reduced toxicity to normal cells, especially even under light irradiation due to the self-quenched state of VPFs in PNPs.[28] Thereafter, the cell death pattern with PNPs^{+LED} treatment was determined via Annexin V and PI dual staining. It has been reported that PDT with strong laser irradiation can cause tumor necrosis due to the excessive generation of ROS which causes unregulated cell death, resulting in reduced therapeutic responses.[29] However, the viabilities of U87 and C6 cells after PNPs^{+LED} treatment were ≈14 – 18% and all dead cells exhibited early apoptotic patterns (Figure 3h). The death pattern by VPF^{+LED} treatment was also early apoptosis in total, indicating that the microLED-mediated photodynamic therapy was effective without inducing severe inflammatory responses by cell necrosis.[30] The microLED-mediated light irradiation could minimize the necrosis rate of cancer cells during the PDT via uniform irradiation with a controlled intensity, which is considered a unique advantage of microLED. The results of in vitro cellular assays successfully demonstrated the high cancer cell-specific efficacy of PNPs and their combined chemo-photodynamic effect with microLED guidance.

2.4. In Vivo Biodistribution and Tumor Accumulation of PNPs in Brain Tumor Xenograft Mice

The biodistribution and tumor-specific accumulation of intravenously administered PNPs were examined using U87 brain tumor xenograft mouse models. For the preparation of mouse models, 1×10^7 U87 cells were inoculated to the left flank of five-week-old male Balb/c nude mice, and VPF or PNPs (5 mg kg^{-1}, based on VPF content) were intravenously injected into them when tumors grew to 150 – 200 mm^3. The in vivo fluorescence imaging system (IVIS) of PNP-injected mice at different time points exhibited a gradual increase in tumor fluorescent signals and reached the highest level at 6 h post-injection due to the tumor accumulation of PNPs (**Figure 4a**). In contrast, the changes in the intratumoral fluorescence of VPF-injected mice for 6 h were ignorable since the physiological stability of VPF was poor thereby the amount of VPF delivered to the tumor tissue was not sufficient. The fluorescence of PNP-treated brain tumor tissues after 6 h was 1.5-fold brighter than that of VPF-treated ones, indicating the tumor-specific accumulation of PNP via the nanoparticle-driven EPR effect (Figure 4b). After 6 h post-injection, ex vivo fluorescence images of extracted tumor tissues further proved the enhanced tumor delivery efficiency of PNPs to VPF, with a 2.4-fold higher fluorescence intensity. In addition, the extracted tumor tissues were sectioned and observed via CLSM, wherein strong fluorescent signals of both VPF and DOX were uniformly detected throughout the PNP-treated tumor tissue (Figure 4c). The VPF-treated tumor tissue showed only weak fluorescence of VPF, 9.8-fold lower than the PNP-treated one (**** $p < 0.0001$) (Figure S6, Supporting Information). The biodistribution of intravenously injected VPF and PNPs was investigated via the ex vivo fluorescence imaging of normal organs, discovering the undesirable delivery of excessive VPF to the liver, lung, and kidney due to their hydrophobicity and poor physiological stability (Figure 4d).[31] VPFs distributed in the normal organs were gradually metabolized or excreted and their fluorescence signal was diminished at 48 and 72 h post-administration (Figure S7, Supporting Information). In comparison, PNPs showed a much-reduced distribution to those organs and enhanced tumor accumulation. Notably, neither VPF nor PNPs were delivered to the normal brain tissues since the tight BBB prevented the transportation of substances with molecular weights over 400 – 600 Da (Figure 4e).[32] The CLSM images of normal organ sections also demonstrated the considerable accumulation of VPF in the liver and kidney, whereas lower levels of PNPs were observed in those organs (Figure 4f). The fluorescent signals of PNPs were lower than those of VPFs in all normal organs, and especially, 6.1- and 24.0-fold lower in the liver and kidney, respectively (Figure 4g). The reduction in the undesirable off-target distribution of PNPs compared to VPFs would greatly mitigate the phototoxicity of photosensitizers in PDT. Meanwhile, the PNP accumulation level in tumor tissues was 131.4-fold higher than that of VPF, showing the passive tumor targetability of PNPs. However, both VPF and PNPs were rarely found in brain tissues as they exhibited the lowest fluorescence intensities (Figure S8, Supporting Information). Through the in vivo biodistribution assay, the tumor-specific targetability of PNPs was fully validated, which was expected to promote successful brain tumor therapy with the application of microLEDs.

2.5. In Vivo Therapeutic Effect of MicroLED-Mediated PDT with PNP Against Brain Tumor Xenograft Mice

Before the application of the microLED and PNPs to orthotopic brain tumors, their therapeutic efficacy was first evaluated against tumor xenograft mouse models. Five-week-old male Balb/c nude mice with U87 tumors xenografted on their left flanks (50 – 75 mm^3) were intravenously treated with free DOX (4 mg kg^{-1}), VPF (5 mg kg^{-1}), or PNPs (4 mg kg^{-1} based on DOX

© 2024 The Author(s). Advanced Functional Materials published by Wiley-VCH GmbH

16163028, 2024, 30, Downloaded from https://onlinelibrary.wiley.com/doi/10.1002/adfm.202316386 by Ewha Womans University Library, Wiley Online Library on [10/11/2024]. See the Terms and Conditions (https://onlinelibrary.wiley.com/terms-and-conditions) on Wiley Online Library for rules of use; OA articles are governed by the applicable Creative Commons License

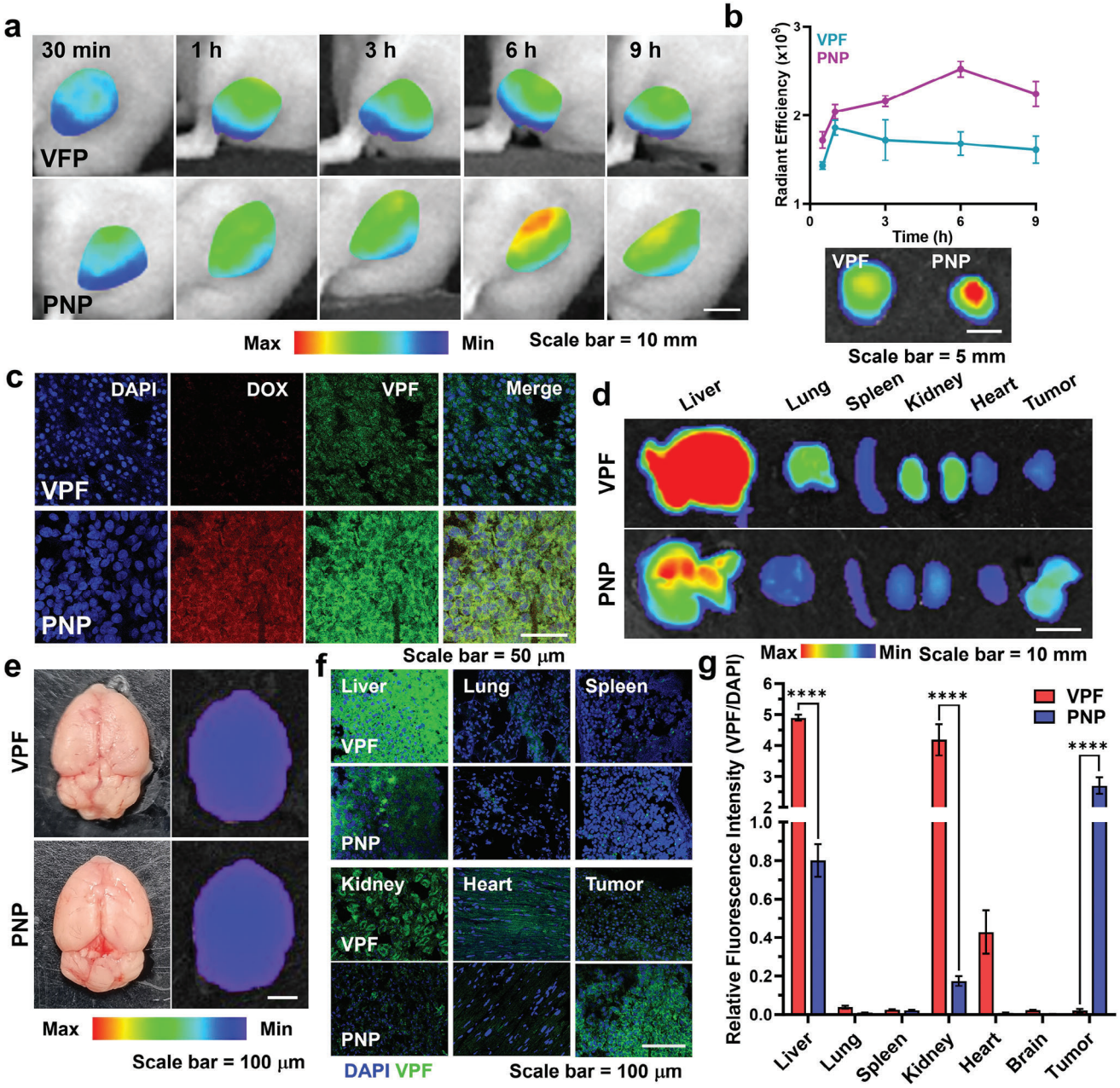


Figure 4. In vivo biodistribution of intravenously administered PNPs in U87 glioma xenograft mice. a) In vivo fluorescent images of U87 glioma-bearing mice to monitor the tumor accumulation of intravenously administered VPFs and PNPs (5 mg kg^{-1}, respectively, based on VPF content) over 6 h. b) Quantification of the time-dependent changes in intratumoral fluorescent intensities by VPFs and PNPs and ex vivo fluorescent images of VPF- or PNP-administered tumor tissues. c) CLSM images of excised tumor tissues showing the tumor accumulation of VPFs and PNPs. d) ex vivo fluorescent images of excised normal organs to determine the biodistribution of intravenously administered VPFs and PNPs. e) ex vivo digital and fluorescent images of excised normal brains, without undesirable delivery of VPFs or PNPs. f) CLSM images of excised normal organs and tumor tissues showing the non-target delivery and tumor accumulation of VPFs and PNPs, and g) their quantification analysis ($n = 3$, **** $p < 0.0001$).

and 5 mg k^{-1}g based on VPF content), irradiated with light 6 h after the drug injection for 1.5 h using the microLED, and monitored to inspect the changes in their tumor volumes for 16 days. The therapeutic procedures were carried out once at the beginning and the tumor volumes were measured once per 2 days. For light irradiation, the needle-type tip of the microLED was implanted precisely into the center of tumor tissues after punching a pinhole with a 26 G sterilized needle, and a light intensity of 50 mW was irradiated for 1.5 h using microLED (**Figure** 5a). During the observation period of 16 days post-treatment, the tumor growth was most effectively suppressed by the PNP^{+LED} treatment. The terminal volume of PNP^{+LED}-treated tumor tissues

© 2024 The Author(s). Advanced Functional Materials published by Wiley-VCH GmbH

16163028, 2024, 30, Downloaded from https://onlinelibrary.wiley.com/doi/10.1002/adfm.202316386 by Ewha Womans University Library, Wiley Online Library on [10/11/2024]. See the Terms and Conditions (https://onlinelibrary.wiley.com/terms-and-conditions) on Wiley Online Library for rules of use; OA articles are governed by the applicable Creative Commons License

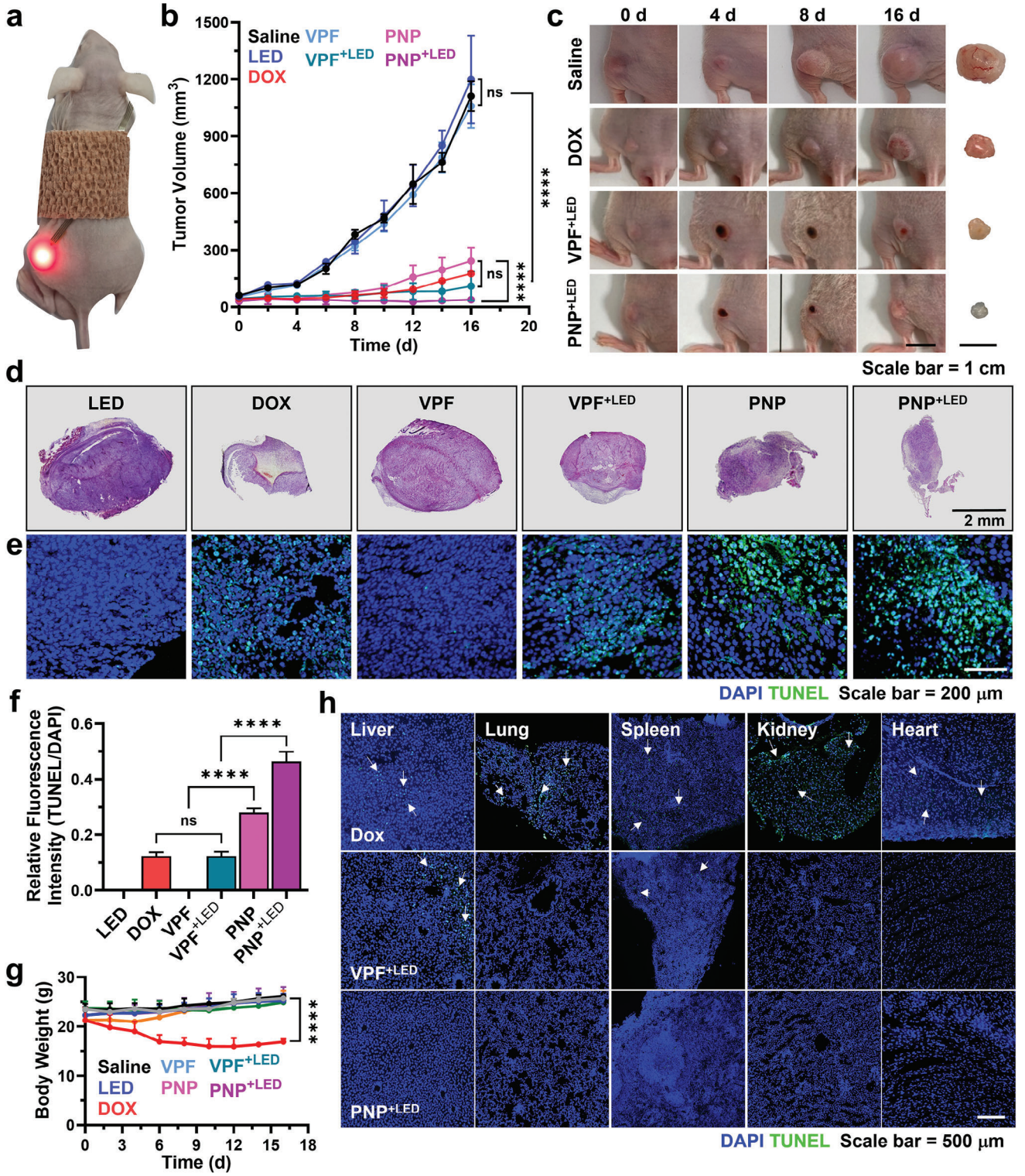


Figure 5. In vivo therapeutic efficacy of microLED-mediated chemo-photodynamic therapy with PNP administration against U87 glioma xenograft mice. a) A digital image presenting the actual implantation of microLED to xenografted U87 glioma tissues. b) The tumor growth curves upon the treatment of DOX (3 mg kg^{-1}), VPF (4 mg kg^{-1}), and PNPs (3 mg kg^{-1}, based on DOX content) with or without light irradiation over 16 days ($n = 3$). **c)** Digital images of tumors treated with saline, DOX, VPF^{+LED}, and $PNPs^{+LED}$ at 0, 4, 8, and 16 days post-treatment, and excised tumor tissues showing their terminal sizes. d) The H&E staining histological images of tumor sections 3 days after the treatment. e) TUNEL assay of tumor tissues excised 3 days after the treatment to observe the tumor apoptosis, and f) their quantification data ($n = 3$). g) Changes in body weights of recipient mice during the therapy and monitoring ($n = 3$). h) TUNEL assay of excised normal organs after finishing therapeutic procedures and monitoring to determine the off-target toxicity (white arrows = apoptotic area). ns = not significant, **** $p < 0.0001$.

© 2024 The Author(s). Advanced Functional Materials published by Wiley-VCH GmbH

16163028, 2024, 30, Downloaded from https://onlinelibrary.wiley.com/doi/10.1002/adfm.202316386 by Ewha Womans University Library, Wiley Online Library on [10/11/2024]. See the Terms and Conditions (https://onlinelibrary.wiley.com/terms-and-conditions) on Wiley Online Library for rules of use; OA articles are governed by the applicable Creative Commons License

was 38.16 ± 9.45 mm^3, not much different from their initial volume, and 29-fold smaller than the saline-treated mice (**** $p < 0.0001$) (Figure 5b). The tumors treated with saline, light only, and VPF only without light rapidly grew up to around 1100 – 1200 mm^3, exhibiting no statistical difference from one another (Figure 5c; Figure S9, Supporting Information). The treatment of VPF^{+LED}, DOX, and PNPs without light also efficiently inhibited tumor growth, but the sizes of those tumors slightly increased to 2.4 −6.1-fold compared to the initial volumes. It was considered that the superior tumor-suppressing property of PNP^{+LED} treatment was attributed to the synergistic activity of chemotherapy and PDT, wherein the ROS generated by VPF and microLED-mediated irradiation not only directly damaged tumor tissues but also enhanced the sensitivity of cancer cells to DOX.[33] The passive tumor targetability of PNPs would positively affect their antitumor efficacy as well. When the tumors were excised at 3 days post-treatment and assessed with histological analysis, apparent damages were detected in tumor tissues treated with PNP^{+LED} compared to those irradiated with light only (Figure 5d). Their sizes were about a quarter of light-treated ones, and the H&E staining of sections was not clear due to severe cell death. Those treated with DOX, VPF^{+LED}, and PNPs without light were found to be moderately damaged as well. Moreover, the TUNEL assay of tumor tissues more clearly visualized their apoptosis (Figure 5e). PNP^{+LED}-treated tumor tissues exhibited the strongest TUNEL fluorescence intensity, which was encouraged by the tumor-specific accumulation of PNPs and the cooperative chemo-photodynamic effect using the PNPs and microLED. The TUNEL fluorescent signal from PNP^{+LED}-treated tumor tissues was 1.7 – 3.8-fold brighter than those from DOX, VPF^{+LED}, and only PNP-treated ones (**** $p < 0.0001$) (Figure 5f). Tumor tissues treated with PNP only also expressed a 2.3-fold higher apoptotic signal than those with DOX or VPF^{+LED} treatment, indicating the enhanced tumor delivery efficiency of PNPs (**** $p < 0.0001$). However, no apoptotic signal was found in only LED- and only VPF-treated tumors. Importantly, the mice treated with all different therapeutic procedures except DOX did not exhibit any notable body weight loss since PNPs were highly tumor-specific and VPF was activated only at the region of irradiation (Figure 5g). As expected, DOX-treated mice gradually lost weight due to the significant systemic toxicity of DOX (**** $p < 0.0001$). Intravenously administered DOX was undesirably distributed to normal organs and caused their apoptosis (white arrows), in particular, the lung and kidney were observed to be damaged by DOX the most (Figure 5h). On the contrary, other treatments including PNP^{+LED} did not induce the apoptosis of normal organs, confirming the safety of their systemic administration. The tumor-exclusive light irradiation by microLED was also considered to mitigate their toxicity. Moreover, the hematological analysis of Balb/c mice after the intravenous administration of PNPs (5 mg kg^{-1} based on VPF content) did not show any significant changes in the concentrations of blood components compared to those before the administration, suggesting that PNPs rarely affect the function of liver and kidney (Figure S10, Supporting Information). Therefore, PNPs with microLED were proven to be appropriate for the treatment of brain tumors in points of their therapeutic efficacy and negligible side effects.

2.6. In Vivo Therapeutic Effect of MicroLED-Mediated PDT with PNP Against Brain Tumor Orthotopic Rats

The therapeutic efficacy of microLED-mediated chemo-photodynamic therapy with PNPs was finally assessed in the orthotopic brain tumor models and compared to those of PNP treatment without light irradiation and PNP treatment with conventional laser-based irradiation (PNP^{+Laser}). Digital images were provided to describe the tumor implantation, microLED application, and treatment procedures for rat models (**Figure 6a**). Briefly, glioma rat models were prepared by implanting 1×10^5 C6 cells to the cortex located 2.3 mm lateral to the bregma of six-week-old male Sprague-Dawley (SD) rats, and the growth of tumor tissues was monitored via MRI and whole brain histology. The aggressive proliferation feature of glioma tissues inside the brain was observed in the MRI and H&E images, wherein massive lumps severely invading the corpus callosum and putamen were formed within 3 weeks (Figure 6b). The initial tumor sizes to conduct PNP^{+LED} treatment were regulated to be ≈5 mm^3, which was confirmed via 3D MRI scanning of the rat head (tumor volume = *x*-axis diameter x y-axis diameter x z-axis diameter x $\pi/6$) (Figure 6c). Thereafter, PNPs (10 mg kg^{-1}, based on VPF content) were intravenously administered to the brain tumor-bearing rats at 9 and 11 days after the tumor implantation. The IVIS images of PNP-administered rats showed that the PNPs circulated with the bloodstream, were increasingly transported to blood vessels in the brain, and reached their highest levels at 6 h post-injection (Figure 6d). When the brains were extracted and their ex vivo fluorescence images were obtained 6 h after the intravenous administration of PNPs, it was determined that administered PNPs were accumulated exclusively inside the tumor tissues due to the disrupted BBB by angiogenic vessels in tumor tissues, whereas their delivery to normal brain tissues was thoroughly restricted (Figure 6e; Figure S11, Supporting Information).[34] More precisely analyzing the whole section of brain tissues via confocal microscopy, the bright fluorescence signal of PNPs (green color) was concentrated mainly in tumor tissues containing many angiogenic vessels stained with CD31 (red color) while rarely found in normal brains (Figure 6f). The fluorescence of PNPs was clearly visible not only in highly vascularized tumor regions but also in deep tumor areas, suggesting the uniform diffusion of PNPs throughout whole tumor tissues due to hyperangiogenesis.[35] As the tumor growth proceeded from 1 to 2 weeks, the disruption of BBB in tumor tissue was clearly increased, leading to more PNPs being distributed in deep tumor tissues, indicating that the intravenously injected PNPs can be localized in tumor tissues through nanoparticle-derived enhanced permeability and retention (EPR) effect (Figure S12, Supporting Information).[36] In addition, the CLSM images of the tumor and normal brain tissues after Claudin 5 and VE-cadherin staining showed that normal blood vessels maintained their morphology with regularly oriented tight junctions, confirming the presence of rigid BBB (Figure 6g,h; Figure S13, Supporting Information). Intravenously injected PNPs remained inside blood vessels (white arrows) by BBB rather than diffuse into brain tissues. On the contrary, the blood vessels in tumor tissues had relatively disordered sectional morphology and loose

© 2024 The Author(s). Advanced Functional Materials published by Wiley-VCH GmbH

16163028, 2024, 30, Downloaded from https://onlinelibrary.wiley.com/doi/10.1002/adfm.202316386 by Ewha Womans University Library, Wiley Online Library on [10/11/2024]. See the Terms and Conditions (https://onlinelibrary.wiley.com/terms-and-conditions) on Wiley Online Library for rules of use; OA articles are governed by the applicable Creative Commons License

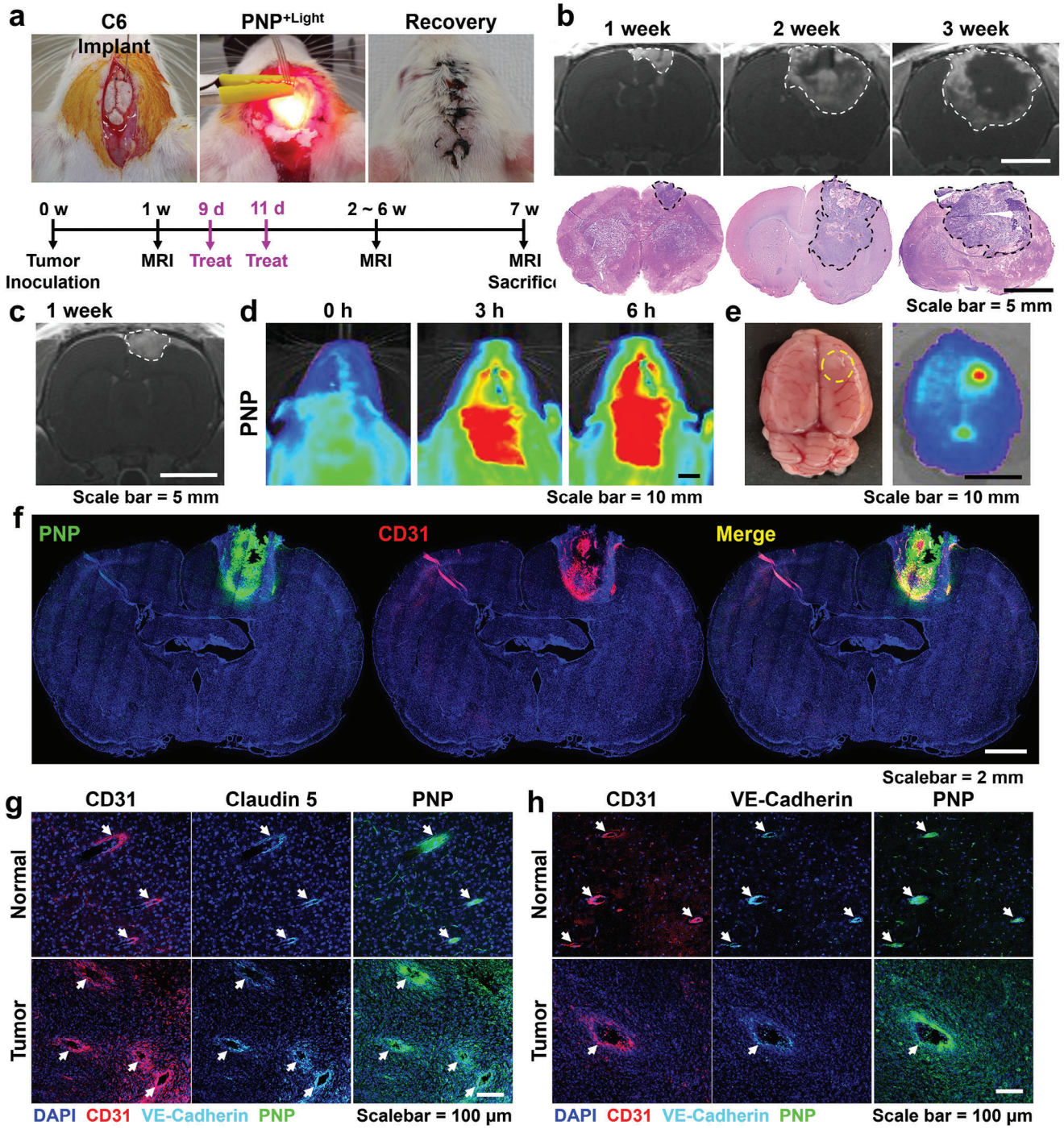


Figure 6. In vivo therapeutic efficacy of microLED-mediated chemo-photodynamic therapy with PNPs against C6 glioma orthotopic rats. a) Digital images describing the procedure of C6 brain tumor orthotopic implantation and microLED application, and the experimental plan for the microLED-mediated therapeutic procedure and monitoring. b) In vivo MR and ex vivo H&E histological images of rat brains 1 – 3 weeks after the orthotopic glioma implantation (dashed line = tumor tissue). c) In vivo MR image of rat brain with the implanted glioma tissue right before starting the treatment procedures (1 week, white dashed line = tumor tissue). d) In vivo fluorescent images of rat heads over 6 h after the intravenous administration of PNPs (10 mg kg^{-1}, based on DOX content). e) ex vivo digital and fluorescence images of the C6 glioma-implanted brain tissue. f) ex vivo whole-sectional CLSM images of the glioma-implanted (1-week post-inoculation) brain after the intravenous PNP administration, stained with DAPI and CD31. CLSM images of PNP-treated normal brain and glioma tissues (1-week post-inoculation) after staining with g) DAPI, CD31, and Claudin 5, or h) DAPI, CD31, and VE-cadherin, showing blood vessels and tight junction (white arrows = blood vessels).

© 2024 The Author(s). Advanced Functional Materials published by Wiley-VCH GmbH

16163028, 2024, 30, Downloaded from https://onlinelibrary.wiley.com/doi/10.1002/adfm.202316386 by Ewha Womans University Library, Wiley Online Library on [10/11/2024]. See the Terms and Conditions (https://onlinelibrary.wiley.com/terms-and-conditions) on Wiley Online Library for rules of use; OA articles are governed by the applicable Creative Commons License

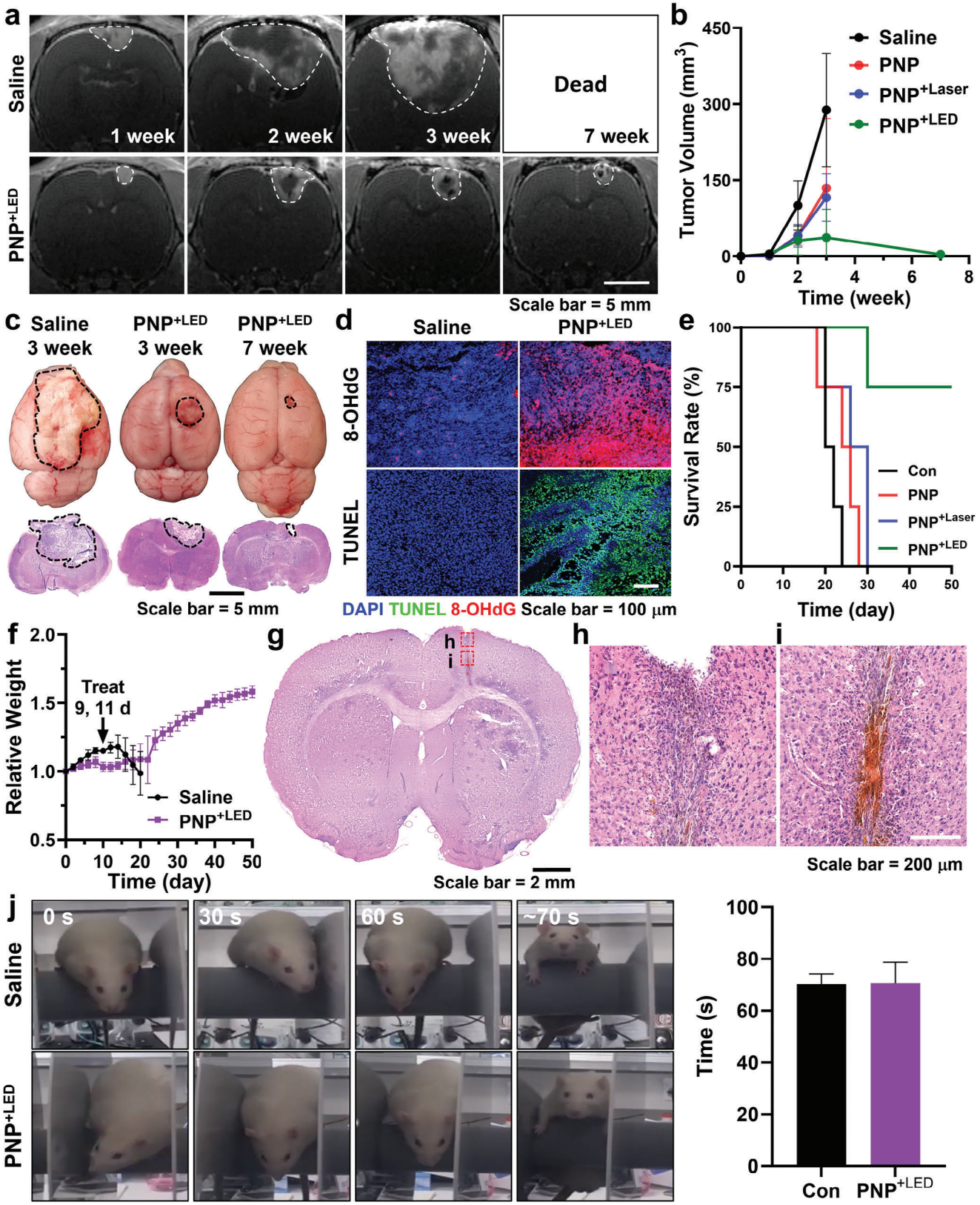
junction, thereby a considerable amount of PNPs spread from vessels into the tumor tissues.

Based on the imaging results, 6 h post-administration of PNPs, the scalp of recipient rats was incised, and their skulls were punctured at the site of tumor tissues for light irradiation using the microLED or conventional laser through the holes. MicroLED was implanted in the center of tumor tissues through the punctured area to irradiate light (50 mW) for 30 min. This is because rats died when anesthetized for more than 30 min, so the maximum radiation time was determined to be 30 min. As a control experiment, the tumors were also illuminated using a conventional laser (637 nm, 50 mW, 30 min) 6 h after the administration of PNPs (PNP^{+Laser}). MicroLED was smoothly introduced into the brain tumor tissues with minimal invasiveness and effectively delivered light sources inside the skull. After the treatment, the changes in tumor sizes were monitored via MRI once a week for up to 7 weeks. The MRI images of the brains exhibited the rapid growth of saline-treated tumor tissues occupying a large area of the brains within 3 weeks, whereas those with PNP^{+LED} treatment gradually regressed without further growth for 7 weeks (**Figure** 7a; Figure S14, Supporting Information). The PNP-only or PNP^{+Laser} treatment showed moderate tumor growth suppression but was not very effective compared to the PNP^{+LED} treatment. Notably, the sizes of tumors treated with PNP and PNP^{+Laser} were not much different from each other since the external light by laser could not reach the tumor tissues through the skull, and the PDT effect was not activated. The sizes of saline-treated tumors 3 weeks after inoculation were 288.34 ± 91.27 mm^3, 7.9-fold larger than PNP^{+LED}-treated ones during the same experimental period (Figure 7b). Tumors treated with PNP only or PNP^{+Laser} grew to 134.12 ± 111.97 and 115.75 ± 33.00 mm^3 for 3 weeks, respectively, which were 3.2 – 3.7-fold larger than PNP^{+LED}-treated tumors. Only the PNP^{+LED} treatment successfully activated chemo- and photodynamic combined therapeutic effects via sufficient light delivery to deep tumor tissues by microLED implantation. Moreover, the tumoral regions with PNP^{+LED} treatment were further diminished and their sizes after 7 weeks were measured as 3.80 ± 1.97 mm^3. In the digital images of excised brains, the saline-treated tumors (black dashed line) widely spread throughout the cerebrum thereby the original morphology of the normal brain was severely destructed (Figure 7c). On the contrary, the tumors with PNP^{+LED} treatment at 3 weeks were much smaller than saline-treated ones, and only small dimples were visible after 7 weeks. The whole-slide H&E histology assay of the brains more clearly showed their tumoral regions, wherein a large area of tumor tissues with irregular morphologies and strong hematoxylin staining was visible in saline-treated brains due to the uncontrolled proliferation of glioma.[37] A considerable portion of the brain was covered with tumor tissues, making it challenging to distinguish the corpus callosum, hippocampus, and even the substructure such as basal ganglia. These massive sizes of tumors brought about elevated intracranial pressure, resulting in pronounced displacement of surrounding normal brain tissues.[38] This was considered a primary factor contributing to the mortality observed in the saline-treated group, typically occurring within ≈3 weeks. In the histology images of PNP^{+LED}-treated brains after 3 weeks, a large indentation was detected inside the tumoral regions rather than filled with tumor tissues, and the indentation was almost recovered after 7 weeks as well. No tumor tissues were found in the PNP^{+LED}-treated brains after 7 weeks. The TUNEL assay of PNP^{+LED}-treated brains after 3 weeks exhibited broad apoptotic regions in the center of tumor tissues, which was not found in saline-treated ones, attributed to the implantation of the microLED at the tumor centers and its therapeutic effect together with the administered PNPs (Figure S15, Supporting Information). The application of microLED and PNPs effectively induced tumor apoptosis, while they did not impair the normal brain tissues. The apoptotic area inside the PNP^{+LED}-treated tumor tissues was not detected any longer at 7 weeks post-treatment, remaining only a small cavity. When comparing the CLSM images of tumor tissues with TUNEL and 8-hydroxy-2′ -deoxyguanosine (8-OHdG) staining 3 weeks after the treatment, PNP^{+LED} treatment was confirmed to induce strong and uniform oxidative DNA damage inside the tumor due to the cooperative activity of DOX and ROS generation, leading to extensive tumor apoptosis (Figure 7d). Encouraged by effective chemo-photodynamic therapy with microLED and PNPs, 80% of treated rats survived over 7 weeks (Figure 7e). However, no saline-treated rats could survive more than 26 days due to the serious tumor invasion into brain tissues and loss of normal integrity. All rats treated with PNPs only or PNP^{+Laser} also died within 30 days due to the insufficient therapeutic effect.

Subsequently, the possible adverse effects of PNP administration and microLED implantation on brains and other normal organs were investigated. Monitoring the body weight changes of recipient rats during the experimental period, the treatment of PNP^{+LED} did not induce any significant weight loss (Figure 7f). Although there was a slight decrease in body weights of PNP^{+LED}-treated right after the therapy, it immediately recovered and they gradually gained weight for the last 40 days of observation. Meanwhile, saline-treated rats exhibited acute weight loss starting 16 days after tumor transplantation, attributed to the aggressive progression of glioma. The histologic analysis of normal organs was further carried out upon completing the therapy and monitoring, discovering that all normal organs from PNP^{+LED}-treated rats were preserved with their normal integrities without any remarkable damage similar to saline-treated ones due to the inactiveness of PNPs inside the normal tissues with low cathepsin B levels (Figure S16, Supporting Information). The biocompatibility and thermal toxicity of microLED were also assessed by implanting it into normal brain tissues and keeping it turned on for 30 min. In the MR images of brains after the microLED implantation and light irradiation, a small stab wound whose size was similar to that of the microLED guide needle was detected right at the site of microLED implantation, and the volume of the wound was measured as 0.07 ± 0.001 mm^3 (Figure S17a,b, Supporting Information). In addition, the temperature of the microLED-implanted brain tissue area was not changed during the 30-min light irradiation, indicating that the microLED had a low risk of causing any heat-associated adverse effect (Figure S17c, Supporting Information). As closely examining the stab wound through the H&E histology analysis of brain tissues, the injured site was strictly localized to where the microLED was inserted and not spread to adjacent regions (Figure 7g). The magnified histological images of microLED-implanted sites more clearly showed that the surrounding brain tissues maintained their original morphologies without any burning, inflammation, or infection (Figure 7h,i).

© 2024 The Author(s). Advanced Functional Materials published by Wiley-VCH GmbH

16163028, 2024, 30, Downloaded from https://onlinelibrary.wiley.com/doi/10.1002/adfm.202316386 by Ewha Womans University Library, Wiley Online Library on [10/11/2024]. See the Terms and Conditions (https://onlinelibrary.wiley.com/terms-and-conditions) on Wiley Online Library for rules of use; OA articles are governed by the applicable Creative Commons License



© 2024 The Author(s). Advanced Functional Materials published by Wiley-VCH GmbH

16163028, 2024, 30, Downloaded from https://onlinelibrary.wiley.com/doi/10.1002/adfm.202316386 by Ewha Womans University Library, Wiley Online Library on [10/11/2024]. See the Terms and Conditions (https://onlinelibrary.wiley.com/terms-and-conditions) on Wiley Online Library for rules of use; OA articles are governed by the applicable Creative Commons License

16163028, 2024, 30, Downloaded from https://onlinelibrary.wiley.com/doi/10.1002/adfm.202316386 by Ewha Womans University Library, Wiley Online Library on [10/11/2024]. See the Terms and Conditions (https://onlinelibrary.wiley.com/terms-and-conditions) on Wiley Online Library for rules of use; OA articles are governed by the applicable Creative Commons License

Although small bleeding was observed in the area of microLED implantation, it posed no significant issue as we intended to implant the device within the tumor. Particularly in clinical applications, the use of CT and MR imaging during operational planning would significantly reduce the risk of damage in blood vessels and adjacent normal tissues. Thus, our results demonstrate that the microLED is highly biocompatible and the brain damage caused by its heat generation is negligible. 7 weeks after the treatment of PNP^{+LED}, the movement of recipient rats was evaluated through a rotarod test and compared to that of tumor-free normal ones (Figure 7j; Videos S1 and S2, Supporting Information). The PNP^{+LED}-treated rats lasted on the rotating apparatus for 70.7 ± 6.6 s, exhibiting no significant difference from the normal rats (70.3 ± 3.1 s). These results fully assured the safety and biocompatibility of both PNPs and microLED not only locally but systemically as well. Finally, microLED-mediated chemo-photodynamic therapy with PNP administration was determined as an effective approach for glioma treatment, with minimal invasiveness, efficient light irradiation inside the deep tumor tissues, strong therapeutic efficacy, and relief of side toxicity.

3. Conclusion

In this study, a minimally invasive implantable microLED and cathepsin B-cleavable prodrug nanoparticles (PNPs) were employed for the chemo-photodynamic combination therapy of glioma. The needle-type implantable microLED could apply light for photodynamic therapy into the center of tumor tissues beneath the skull in a minimally invasive way, successfully irradiating throughout the whole tumor tissue to overcome the short tissue penetration depth of conventional irradiation devices. The light or heat from the implanted microLED did not impair the surrounding tissues during its long-term application over 2 h, and its light intensity was freely controllable. PNPs were self-assembled into nanoparticles with stable dispersity in physiological conditions, and they exhibited high inertness to normal tissues with low cathepsin B expression. They were cathepsin B-specifically cleaved inside cancer cells to release free DOXs and VPFs, eliciting strong chemo-photodynamic efficacy under light irradiation. The application of PNPs with microLED-mediated light irradiation showed enhanced therapeutic efficacy compared to the single therapy of DOXs or VPFs due to their synergistic effect. When intravenously administered to brain tumor models, PNPs could be selectively delivered to tumor tissues due to the leaky BBB, while they were not accumulated in normal brains. The microLED was smoothly implanted into the center of orthotopic glioma tissues through a small pinhole and successfully delivered light inside the skull. The microLED-mediated chemo-photodynamic therapy with PNP administration exhibited remarkable therapeutic efficacy against glioma, and neither microLED nor PNP induced any significant side effects on normal tissues. Notably, the synergistic effect of chemo-photodynamic therapy was maximized under the microLED guidance as VPFs from PNPs could tumor-specifically generate sufficient ROS, causing tumor tissues to be highly susceptible to DOX treatment. In conclusion, chemo-photodynamic therapy with microLED and PNPs would be a potent method for glioma treatment, favorably complementing the limitations of photodynamic therapy.

4. Experimental Section

Materials: Poly(methyl methacrylate) (PMMA A2), poly(pyromellitic dianhydride-co-4,4-oxydianiline) (PI, amic acid solution), copper etchant, *N,N*-diisopropylethylamine (DIPEA), 1-ethyl-3-(3-dimethylaminopropyl)carbodiimide (EDC), *N*-hydroxysuccinimide (NHS), dichlorodihydrofluorescein diacetate (DCFH-DA), chloroform, anhydrous *N,N*-dimethylformamide (DMF), dimethyl sulfoxide (DMSO), annexin V/PI staining kit, and 1,3-diphenylisobenzofuran (DPBF) were obtained from Sigma-Aldrich (St. Louis, MO, USA). SU-8 (SU-8 2) and SU-8 (SU-8 100) were purchased from Micro Resist Technology (Berlin, Germany) and MicroChem Inc. (Chungcheongbuk-do, Republic of Korea), respectively. Polysiloxane acrylate (PSA) precursor (ST1010s) was commercially available from MCNet Inc. (Gwangju, Republic of Korea) and poly(acrylic acid) (PAA) was obtained from Polysciences (Warrington, UK). AZ GXR 601 positive photoresist and AZ nLOF 2070 negative photoresist were acquired from NM Tech (Incheon, Republic of Korea) and MicroChemicals (Ulm, Germany), respectively. Doxorubicin hydrochloride (DOX), verteporfin (VPF), and *Phe-Arg-Arg-Gly* (FRRG) were purchased from FutureChem (Seoul, Republic of Korea). Ham's F-12K (Kaighn's) medium (F-12K) and Quanti-Max WST-8 cell viability assay kit (WST-8) were available from Thermo-Fisher Scientific (Waltham, MA, USA) and BIOMAX (Gyeonggi-do, Republic of Korea), respectively. RPMI 1640, Dulbecco's modified eagle medium (DMEM), and fetal bovine serum (FBS) were obtained from Welgene Inc (Gyeongsangbuk-do, Republic of Korea). Recombinant human cathepsin B protein and TUNEL assay kit were purchased from R&D systems (Minneapolis, MN, USA). Monoclonal anti-mouse cathepsin B antibody was acquired from Santa Cruz Biotechnology (Dallas, TX, USA), and monoclonal anti-mouse β-actin antibody and hematoxylin and eosin (H&E) staining kit were obtained from Abcam (Gyeonggi-do, Republic of Korea). All chemicals were used as received without additional purification.

Instruments: The microscopic structure and dimension of fabricated microLED were observed through a field emission-scanning electron microscope (FESEM; JSM-IT800, JEOL Ltd, Tokyo, Japan). The input voltage and power for the microLED operation were supplied and controlled with a power supply (DP 30-03TP, Toyotech, Incheon, Republic of Korea), and the optical and electronic properties of the microLED were examined using a light spectrometry (HR4000, Ocean Optics Inc., Orlando, FL, USA) and probe station (MST 5500B, MS Tech., Seoul, Republic of Korea), respectively. An infrared camera (T420, FLIR System Inc., Wilsonville, Oregon, USA) was employed to measure the temperature change of in vivo brain and ex vivo brain tumor tissues during the microLED application. The hydrodynamic diameter and long-term dispersion stability of

Figure 7. Safety and biocompatibility of microLED implantation and PNP treatment against rat models. a) Follow-up MR images of C6 glioma-implanted rat brains over 7 weeks after the treatment of saline or $PNPs^{+LED}$ (10 mg kg^{-1}, based on DOX content) with microLED-mediated light irradiation (white dased line = tumor tissues). b) Changes in tumor volumes over 7 weeks after the treatment of saline, PNPs, $PNPs^{+Laser}$, or $PNPs^{+LED}$, analyzed via MRI. c) Digital images and H&E staining histological images of excised brains treated with saline or $PNPs^{+LED}$, after 3 or 7 weeks (black dashed line = tumor tissues). d) CLSM images of TUNEL- or 8-OHdG-stained tumor tissues 3 weeks after the treatment of saline or $PNPs^{+LED}$. e) The survival rates of recipient rats during the therapeutic and monitoring periods. f) 50-day body weight changes of saline- or PNP^{+LED}-treated rats. g) Histological analysis of whole brain tissues after the microLED application and 30 min-light irradiation, and its magnified images at h) the middle and i) end of the implanted regions. j) Rotarod test with saline- or PNP^{+LED}-treated rats 50 days post-treatment.

© 2024 The Author(s). Advanced Functional Materials published by Wiley-VCH GmbH

PNPs were analyzed via dynamic light scattering (DLS; Zetasizer Nano ZS, Malvern Instruments, Worcestershire, UK), and their size and morphology were further confirmed using transmission electron microscopy (TEM; CM-200, Philips, Amsterdam, Netherlands). The comparison of ultraviolet (UV) and visible light (vis) absorption spectra of DOX, VPF, and PNP was carried out via UV-vis light spectrophotometry (UV-vis; Agilent Cary 300; Agilent Technologies, Santa Clara, CA, USA). For the confirmation of VPF-FRRG-DOX synthesis and its cathepsin B-specific cleavage, a reverse-phase high-performance liquid chromatography and mass spectrometry (RP-HPLC/MS; 1260 Infinity II LC system, Agilent Technologies, Santa Clara, CA, USA) was utilized. The cathepsin B expression levels in normal and brain cancer cells were measured using a western blot reader (iBright CL750; Thermo Fisher Scientific, Waltham, MA, USA), and a confocal laser scanning microscopy (CLSM; Leica TCS SP8, Leica Microsystems GmbH; Wetzlar, Germany) and a fluorescence microscope (EVOS M7000, Thermo Fisher Scientific, Waltham, MA, USA) were employed to obtain in vitro cellular fluorescence images. In vitro cytotoxicity assay was conducted using a microplate reader (Infinite M Nano, Tecan., Männedorf, Switzerland). The in vivo and ex vivo fluorescence images of mice and rats were taken with an In Vivo Imaging System device (IVIS; IVIS Lumina III imaging system, PerkinElmer, Waltham, MA, USA), equipped at Ewha Drug Development Research Core Center. The in vivo magnetic resonance imaging (MRI) of rats was assessed via an MRI device (Bruker 9.4T BioSpec 94/20 MRI, Bruker, Billerica, MA, USA). MRI sequence was set as follows: T1-weighted imaging, echo time = 8.06 ms, repetition time = 500 ms, field of view (FOV) = 100, matrix = 144 × 192, slice thickness = 1 mm.

Fabrication and Characterization of Implantable MicroLED: The fabrication process involved two key components: the LED-containing electrodes and the injectable guide needle for the implantable microLED. For the LED-containing part, PMMA and PI layers were sequentially spun onto a rinsed glass substrate, with thicknesses controlled at 5 µm and 50 nm, respectively, and solidified through baking. A thin metallic layer (5 nm Cr / 100 nm Au) was deposited onto the PI layer through thermal evaporation. Electrodes were patterned using GXR-601 photoresist via conventional photolithography methods, followed by the application of an anisotropic conductive adhesive (ACA) on the gold electrodes.[39] Subsequently, four red-light LEDs were aligned on the ACA-coated electrodes using a mask aligner, and SU-8 2, a UV-curable epoxy, was used to encapsulate the circuit part. The red-light LED (120 × 200 µm) was provided by Samsung Electronics (Suwon, Republic of Korea). Residual PMMA and PI were removed via plasma etching with a 100 nm copper etch mask, followed by the elimination of the sacrificial PMMA layer using a copper etchant, resulting in a film-like flexible LED-containing circuit part with a PI substrate. As for the injectable guide needle part, 3wt.% PAA and SU-8 100 epoxy were spun on a clean glass in sequence. The pattern for the injectable guide needle was formed through photolithography. After placing the glass in 80 °C water for 2 h, the injectable guide needle was separated as the PAA layer dissolved. Finally, the flexible LED-containing part was affixed onto the injectable guide needle part using PSA precursor, completing the microLED assembly. Following fabrication, the input current, input power, and output light power of microLED in response to input voltage were measured using a probe station. Additionally, the microLED's light emission spectrum was assessed using light spectrometry. For temperature measurement, the temperature change with time was monitored by an infrared camera. Subsequently, the microLED's operational performance was evaluated in various environments, including air, water, subcutaneous tissues, and brain tumor spheroids. Long-term operation stability and heat generation were examined by keeping the microLED turned on for 30 min or longer in air, water, and tumor spheroids. All microLEDs were sterilized via UV irradiation for 30 min right before their application in vitro or in vivo.

Synthesis of Cathepsin B-Cleavable Verteporfin-Doxorubicin Prodrug (VPF-FRRG-DOX): The cathepsin B-cleavable VPF-FRRG-DOX synthesis was carried out via successive EDC/NHS esterification, as written in the previous report.[23] In brief, VPF (1.00 g, 1.39 mmol), EDC (0.75 g, 3.91 mmol), and NHS(0.50 g, 4.34 mmol) were placed in a 250 mL 2-neck round-bottom flask and dissolved in 100 mL anhydrous DMF, allowed to react by stirring with a magnetic stir bar at 37 °C for 12 h under the dark condition. The NHS-conjugated VPF (VPF-NHS) was separately collected using a C18 column and lyophilized for 2 days. For the FRRG-conjugated VPF (VPF-FRRG) preparation, lyophilized VPF-NHS (1.00 g, 1.23 mmol) and NH_2-FRRG-COOH (1.00 g, 1.87 mmol) were dissolved in 100 mL DMF and the reaction between them was conducted at 37 °C for 12 h under dark conditions. The crude product was passed through a C18 column and lyophilized to obtain pure VPF-FRRG. Subsequently, lyophilized VPF-FRRG (0.80 g, 0.65 mmol), DOX (0.10 g, 0.17 mmol), EDC (0.37 g, 1.93 mmol), and NHS (0.25 g, 2.17 mmol) were added into a 250 mL 2-neck round-bottom flask and dissolved in 100 ml of DMF. The mixture was gently stirred to proceed with the reaction at 37 °C for 24 h under dark conditions. The excessive reactants were removed via a C18 column, resulting in pure VPF-FRRG-DOX after lyophilization. The product for each synthetic step was confirmed through the HPLC (ACN/H_2O co-eluent, gradient elution from 20:80 to 80:20 (v:v), 0.45 mL min^{-1} elution rate, 40 min), and LC/MS analysis.

Formation and Characterization of PNPs: The formulation of PNPs was carried out by dispersing 1 mg VPF-FRRG-DOX prodrugs in 1 mL saline and agitating the solution for 1 min. The size distribution and dispersion stability of PNPs (1 mg mL^{-1}) were analyzed via DLS and their morphology before and after the cathepsin B treatment was observed via TEM. For the cathepsin B cleavage test, PNP (10 µM) was dissolved in MES buffer (0.1 M, pH5.5) and added with cathepsin B enzyme (50 µg mL^{-1}). The mixture was sampled and analyzed via HPLC (ACN/H_2O co-eluent, gradient elution from 20:80 to 80:20 (v:v), 0.45 mL min^{-1} elution rate, 40 min) and LC/MS at 0, 6, 12, and 24 h after the cathepsin B addition to determine the cleavage of PNPs. The UV and visible light absorbance of DOX, VPF, and PNP (10 µM) were measured by UV-vis to compare their absorption spectra. The assessment of the ROS generation profile of VPF, PNP, and cathepsin B-treated PNP (10 µM) was performed by adding DPBF (100 µM) in their solutions, irradiating them for 15 min with microLED (650.6 nm wavelength, 50 mW), and measuring the absorbance intensity at 410 nm wavelength.

In Vitro Cellular Analysis Using PNPs: Rat heart myoblast (H9C2), human glioblastoma (U87), and rat glioma (C6) cells were obtained from the American Type Culture Collection (ATCC; Manassas, VA, USA) and used for in vitro tests. The cathepsin B expression levels of H9C2, U87, and C6 cells were measured by western blot assay and quantified using the Image J program. To assess the cellular uptake behavior of DOX, VPF, and PNP, 5×10^4 H9C2, U87, and C6 cells were separately seeded in confocal dishes and incubated with DOX, VPF, or PNP (5 µM) for 24 h. The cells were then fixed with 4% paraformaldehyde for 15 min and their nuclei were stained with 4′,6-diamidino-2-phenylindole (DAPI) for 15 min at 4 °C to observe via CLSM. The in vitro ROS generation and cell apoptosis induction of DOX, VPF, and PNP were further investigated by culturing 5×10^4 U87 and C6 cells in confocal dishes and incubating them with DOX, VPF, or PNP (5 µM). For the measurement of intracellular ROS generation levels, DCFH-DA (40 µM) was added to the cells and allowed to be taken up by the cells for 1 h. The light was subsequently irradiated to the cells via microLED (50 mW) for 15 min, their nuclei were stained with DAPI for 15 min, and the cells were observed using a fluorescence microscope. For the measurement of apoptotic area, 5×10^4 U87 and C6 cells were seeded, treated with DOX, VPF, or PNP (5 µM), and irradiated using microLED (50 mW) for 15 min. 3 h after the additional incubation, cells were treated with Annexin V for 10 min, stained with DAPI for 15 min, and analyzed with a fluorescence microscope.

To conduct the cytotoxicity assay, H9C2, U87, and C6 cells were seeded in 96-well plates and incubated with DOX, VPF, or PNP (5 µM) for 24 h, followed by microLED-mediated light irradiation at 50 mW for 15 min. After the treatment and light exposure, the cells were washed using DPBS twice and dipped in 0.2 mL cell culture media containing 10% WST-8 solution for 15 min. The cell viability was determined by detecting the colorimetric change (absorbance at 450 nm) of the WST-8 solution with a microplate reader. The apoptosis and necrosis of cancer cells with DOX, VPF, and PNP treatment were determined by staining them with Annexin V (5 µL) and propidium iodide (PI; 10 µL) for 10 min and analyzing them via flow cytometry.

© 2024 The Author(s). Advanced Functional Materials published by Wiley-VCH GmbH

16163028, 2024, 30, Downloaded from https://onlinelibrary.wiley.com/doi/10.1002/adfm.202316386 by Ewha Womans University Library, Wiley Online Library on [10/11/2024]. See the Terms and Conditions (https://onlinelibrary.wiley.com/terms-and-conditions) on Wiley Online Library for rules of use; OA articles are governed by the applicable Creative Commons License

In Vivo Biodistribution and Tumor Accumulation Analysis of PNPs in U87 Tumor-Bearing Mice: All mice were fed in the specific-pathogen-free (SPF) rooms at the College of Pharmacy, Graduate School of Pharmaceutical Sciences, Ewha Womans University, and all animal tests in this study were carried out according to the guidelines and regulations of the institutional animal care and use committee (IACUC) at Ewha Womans University (approval no. EWHA IACUC 22-073-2). To develop U87 brain tumor-xenograft mouse models, five-week-old male BALB/c nu/nu mice were obtained from NARA Biotech (Seoul, Republic of Korea) and 1×10^7 U87 cells were subcutaneously injected into the left flank of the mice. When the tumor volumes reached 150–200 mm^3, VPF (5 mg kg^{-1}) or PNP (5 mg kg^{-1}, based on VPF content) was intravenously administered to the tumor-bearing mice, and their near-infrared fluorescence (NIRF) images of recipient mice were obtained at 0.5, 1, 3, and 6 h post-administration using IVIS to investigate the biodistribution and tumor accumulation of VPF and PNP. 6, 48, and 72 h after the administration, recipient mice were sacrificed and their organs and tumor tissues were excised to observe their ex vivo fluorescent signals. Subsequently, the collected organs and tumors were further stained with DAPI for CLSM analysis.

In Vivo Therapeutic Efficacy Assessment of PNP with Implantable MicroLED against U87 Tumor Xenograft Mouse Models: To assess the therapeutic efficacy of PNP^{+LED} treatment, U87 tumor-xenograft mice were prepared by inoculating 1×10^7 U87 cells to the left flank of five-week-old male BALB/c nu/nu mice. When the tumor volumes grew to 50 – 75 mm^3, the mice were intravenously administered with DOX (4 mg kg^{-1}), VPF (5 mg kg^{-1}), and PNP (5 mg kg^{-1}, based on VPF content) twice with a 2-day interval. In the cases of VPF^{+LED} and PNP^{+LED} experimental groups, the recipient mice further underwent the implantation of microLED into the center of tumor tissues 6 h after the VPF or PNP administration, and microLED-mediated light irradiation was performed at 50 mW for 90 min. The changes in tumor volumes and body weights were measured every two days for up to 16 days, wherein the tumor volumes were calculated as (shortest diameter)^2 x (longest diameter) x $\pi/6$ ($n = 3$). 5 days after starting the treatment, three mice in each experimental group were sacrificed to extract their tumor tissues, and the extracted tumor tissues were stained with H&E or DAPI/TUNEL for histological or CLSM analysis. After 16 days of monitoring, all recipient mice were sacrificed, their organs and tumor tissues were resected, and then the organs and tumor tissues were stained with DAPI/TUNEL to observe the apoptotic area in them via CLSM. For the hematological assay, Balb/c mice were intravenously treated with PNPs (5 mg kg^{-1} based on VPF content) twice at 2-day intervals and sacrificed 7 days post-administration to extract whole blood from their heart.

In Vivo Therapeutic Efficacy Assessment of PNP with Implantable MicroLED against C6 Tumor Orthotopic Rat Models: All rats were fed in the specific-pathogen-free (SPF) rooms at the Avison Biomedical Research Center (ABMRC), Yonsei University, and all animal tests in this study were carried out according to the guidelines and regulations of IACUC at Yonsei University (approval no. 2023-0137). All rats underwent anesthesia with isoflurane before the experimental procedures. For the preparation of the C6 orthotopic brain glioma rat model, six-week-old male Sprague-Dawley (SD) rats were obtained from Orient Bio (Seoul, Republic of Korea) and fixed the head with a stereotaxic frame. After skin incision, 1×10^5 C6 cells dispersed in 5 µL DPBS were injected slowly (0.75 µL min^{-1}) into their brain tissues after craniotomy: anterior-posterior (AP) 0 mm, medial-lateral (ML) 2.3 mm, and dorsal-ventral (DV) 2 mm from the bregma, and the tumor growth was monitored via MRI. After the tumor tissues grew to ~5 mm^3, PNPs (10 mg k^{-1}g, based on VPF content) were intravenously injected, and the NIRF images of recipient rats were obtained at 0, 3, and 6 h post-injection using IVIS to monitor the time-dependent biodistribution of PNPs. The PNP-treated rats were sacrificed 6 h post-injection to obtain brain tissues, and the brain tissues were subsequently sectioned and observed via CLSM upon staining with DAPI, CD31, Claudin 5, and VE-cadherin, respectively. For the therapeutic procedure, 200 µL saline or PNP (10 mg kg^{-1}, based on VPF content) solution was intravenously administered to brain tumor-bearing rats on the 9th and 11th days after the tumor inoculation. After 6 h of PNP administration, microLED was implanted into brain tumors through a small puncture, and tumor tissues were irradiated at 50 mW for 30 min. As a control group, a conventional laser device (LP637-SF70, Thorlabs Inc., Newton, NJ, USA) was also used to irradiate onto the heads of PNP-injected rats (637 nm, 50 mW, 30 min) and compare the PDT activation efficacy. The changes in tumor volumes after the treatment were observed via T1-weighted MR imaging at 1, 2, 3, and 7 weeks with an intravenous injection of gadolinium-based MRI contrast agents, Gadobutrol (Gadovist; 0.1 mL kg^{-1}, Bayer, Bremen, Germany). The body weights and survival rate of recipient rats were measured every two days. After 3 and 7 weeks of tumor implantation, all recipient rats were sacrificed and their brains were collected for CLSM and histology analysis. Their normal organs including the heart, lung, liver, spleen, and kidney were also extracted at 7 weeks post-tumor implantation, and stained with hematoxylin and eosin (H&E) for the histological assay. Tumor tissues in brains were further conducted with TUNEL and 8-OHdG staining to determine the oxidative stress and following apoptosis induction of PNP^{+LED} treatment via CLSM. 7 weeks after the therapeutic process, the saline- and PNP^{+LED}-treated rats were further examined with a rotarod test using an automated four-lane rotarod (Rat Rotarod, 7750; Ugo Basile, Vittorio, Italy). The test was conducted under an accelerator mode ranging from an initial speed of ≈5 rpm to a maximum of 20 rpm (reached within 300 s), and the duration times taken until the rats fell from the apparatus to the floor were measured.

In Vivo Biocompatibility Test of MicroLED Implantation and Operation against Rat Models: The invasive and thermal damage induced by microLED in normal brain, temperature change, and MRI were recorded, and H&E staining was conducted. To determine the damage in the normal brain caused by the heat generation of microLED, the temperature was measured using an infrared camera, and MRI and H&E were performed. MicroLED was implanted at the same location in the brain (AP: 0 mm, ML: 2.3 mm, DV: 2 mm from bregma) as that for the treatment procedure, and the light was applied at 50 mW for 30 min via microLED. The temperature was measured every 5 min for up to 30 min. 24 h after the light irradiation, T1-weighted MRI images were taken. Afterward, the rats were sacrificed and their brain tissues were collected and stained with H&E for histological analysis.

Statistics: The statistical differences between the two experimental groups were analyzed via the student's t-test and the one-way analysis of variance (ANOVA) test was applied to compare those among three or more groups. The Tukey-Kramer post-hoc test was used to validate the statistical significance among the multiple comparisons. All quantitative experiments were repeatedly conducted at least three times and their results were expressed as average ± standard deviation (SD). The statistical significance was presented in the graphs as asterisks, wherein p-values lower than 0.05 were assumed to have statistical significance (ns $p > 0.05$, * $p < 0.05$, ** $p < 0.01$, *** $p < 0.001$, **** $p < 0.0001$).

Supporting Information

Supporting Information is available from the Wiley Online Library or from the author.

Acknowledgements

J.K., H.K.L., J.P., and S.Ik.J. contributed equally to this work. This work was supported by grants from the Samsung Research Funding & Incubation Center for Future Technology of Samsung Electronics (SRFC-IT1901-16). The authors appreciate the Medical Illustration & Design(MID) team, a member of Medical Research Support Services of Yonsei University College of Medicine, for their excellent support with medical illustration.

Conflict of Interest

The authors declare no conflict of interest.

Data Availability Statement

The data that support the findings of this study are available in the supplementary material of this article.

© 2024 The Author(s). Advanced Functional Materials published by Wiley-VCH GmbH

16163028, 2024, 30, Downloaded from https://onlinelibrary.wiley.com/doi/10.1002/adfm.202316386 by Ewha Womans University Library, Wiley Online Library on [10/11/2024]. See the Terms and Conditions (https://onlinelibrary.wiley.com/terms-and-conditions) on Wiley Online Library for rules of use; OA articles are governed by the applicable Creative Commons License

Keywords

chemo-photodynamic therapy, glioma treatment, microscale LED

Received: March 23, 2024
Revised: June 5, 2024
Published online: June 16, 2024

[1] a) N. A. O. Bush, S. M. Chang, M. S. Berger, *Neurosurg Rev* **2017**, *40*, 1; b) I. Jovčevska, *Front Oncol* **2020**, *10*, 798; c) M. M. Hegde, S. Prabhu, S. Mutalik, A. Chatterjee, J. S. Goda, B. S. Rao, *J. Pharm. Invest.* **2022**, *52*, 49.

[2] a) Q. Sun, R. Xu, H. Xu, G. Wang, X. Shen, H. Jiang, *World J. Surg. Oncol.* **2017**, *15*, 1; b) S. Kannan, A. K. Murugan, S. Balasubramanian, A. K. Munirajan, A. S. Alzahrani, *Biochem Pharmacol* **2022**, *201*, 115090.

[3] a) J. T. Miyauchi, S. E. Tsirka, *J Neurol* **2018**, *265*, 741; b) S. L. Hervey-Jumper, M. S. Berger, *J. Neuro-Oncol.* **2016**, *130*, 269.

[4] a) A. R. Cabrera, J. P. Kirkpatrick, J. B. Fiveash, H. A. Shih, E. J. Koay, S. Lutz, J. Petit, S. T. Chao, P. D. Brown, M. Vogelbaum, *Pract Radiat Oncol* **2016**, *6*, 217; b) T. S. van Solinge, L. Nieland, E. A. Chiocca, M. L. Broekman, *Nat. Rev. Neurol.* **2022**, *18*, 221; c) Y.-S. Zhou, W. Wang, N. Chen, L.-C. Wang, J.-B. Huang, *Oncol Rep* **2022**, *47*, 1; d) S. Mehta, C. L. Cascio, *Cell. Mol. Life Sci.* **2018**, *75*, 385.

[5] a) M. Zhao, D. van Straten, M. L. Broekman, V. Préat, R. M. Schiffelers, *Theranostics* **2020**, *10*, 1355; b) S. Han, Y. Liu, S. J. Cai, M. Qian, J. Ding, M. Larion, M. R. Gilbert, C. Yang, *Br. J. Cancer* **2020**, *122*, 1580; c) B. E. Johnson, T. Mazor, C. Hong, M. Barnes, K. Aihara, C. Y. McLean, S. D. Fouse, S. Yamamoto, H. Ueda, K. Tatsuno, *Science* **2014**, *343*, 189.

[6] a) S. W. Cramer, C. C. Chen, *Front Surg* **2020**, *6*, 81; b) T. Zavadskaya, *Exp Oncol* **2015**, *37*, 234; c) J. Akimoto, *Neurologia medico-chirurgica* **2016**, *56*, 151; d) S. K. Dubey, S. K. Pradyuth, R. N. Saha, G. Singhvi, A. Alexander, M. Agrawal, B. A. Shapiro, A. Puri, *J. Porphyrins Phthalocyanines* **2019**, *23*, 1216.

[7] a) T. J. Dougherty, C. J. Gomer, B. W. Henderson, G. Jori, D. Kessel, M. Korbelik, J. Moan, Q. Peng, *J. Nat. Cancer Inst.* **1998**, *90*, 889; b) D. E. Dolmans, D. Fukumura, R. K. Jain, *Nat. Rev. Cancer* **2003**, *3*, 380; c) C. A. Robertson, D. H. Evans, H. Abrahamse, *J. Photochem. Photobiol., B* **2009**, *96*, 1.

[8] a) B. Q. Spring, I. Rizvi, N. Xu, T. Hasan, *Photochem. Photobiol. Sci.* **2015**, *14*, 1476; b) D. Zhong, H. Wu, Y. Wu, Y. Li, J. Yang, Q. Gong, K. Luo, Z. Gu, *J. Controlled Release* **2021**, *329*, 1210.

[9] a) W. Jerjes, T. Upile, Z. Hamdoon, S. Abbas, S. Akram, C. A. Mosse, S. Morley, C. Hopper, *Lasers Surg Med* **2011**, *43*, 283; b) A. Vaidya, Y. Sun, T. Ke, E. K. Jeong, Z. R. Lu, *Magnetic Resonance in Med.: An Official J. Int. Soc. for Magnetic Resonance in Med.* **2006**, *56*, 761.

[10] a) H. Stepp, T. Beck, T. Pongratz, T. Meinel, F.-W. Kreth, J. C. Tonn, W. Stummer, *Toxicol. and Oncol.* **2007**, *26*, 157; b) X. Zhu, H. Zhou, Y. Liu, Y. Wen, C. Wei, Q. Yu, J. Liu, *Acta Biomater.* **2018**, *82*, 143; c) D. S. Pellosi, L. B. Paula, M. T. de Melo, A. C. Tedesco, *Mol. Pharmaceutics* **2019**, *16*, 1009; d) S. J. Madsen, C. H. Sun, B. J. Tromberg, A. T. Yeh, R. Sanchez, H. Hirschberg, *Photochem. Photobiol.* **2002**, *76*, 411.

[11] a) A. D. Garg, P. Agostinis, *Photochem. Photobiol. Sci.* **2014**, *13*, 474; b) A. Ahmed, S. W. Tait, *Mol Oncol* **2020**, *14*, 2994; c) L. Tan, X. Shen, Z. He, Y. Lu, *Front Oncol* **2022**, *12*, 863107.

[12] a) C. Ash, M. Dubec, K. Donne, T. Bashford, *Lasers Med Sci* **2017**, *32*, 1909. b) S. Mallidi, S. Anbil, A.-L. Bulin, G. Obaid, M. Ichikawa, T. Hasan, *Theranostics* **2016**, *6*, 2458.

[13] a) D. Lee, S. Kwon, S.-y. Jang, E. Park, Y. Lee, H. Koo, *Bioact Mater* **2022**, *8*, 20; b) S. S. Stylli, A. H. Kaye, *J Clin Neurosci* **2006**, *13*, 709; c) Z. Huang, *Technol. Cancer Res. Treat.* **2005**, *4*, 283; d) D. Bechet, S. R. Mordon, F. Guillemin, M. A. Barberi-Heyob, *Cancer Treat. Rev.* **2014**, *40*, 229.

[14] a) E. Sorbellini, M. Rucco, F. Rinaldi, *Lasers Med Sci* **2018**, *33*, 1431; b) I. Kirino, K. Fujita, K. Sakanoue, R. Sugita, K. Yamagishi, S. Takeoka, T. Fujie, S. Uemoto, Y. Morimoto, *Sci Rep* **2020**, *10*, 22017; c) H. Liu, L. Daly, G. Rudd, A. P. Khan, S. Mallidi, Y. Liu, F. Cuckov, T. Hasan, J. P. Celli, *Lasers Surg Med* **2019**, *51*, 345; d) Y. Dong, G. Zhou, J. Chen, L. Shen, Z. Jianxin, Q. Xu, Y. Zhu, *Photodiagn. Photodyn. Ther.* **2016**, *13*, 188.

[15] a) H. Kobayashi, M. Ogawa, R. Alford, P. L. Choyke, Y. Urano, *Chem. Rev.* **2010**, *110*, 2620; b) K. Plaetzer, B. Krammer, J. Berlanda, F. Berr, T. Kiesslich, *Lasers Med Sci* **2009**, *24*, 259; c) O. Karatum, M.-J. Gwak, J. Hyun, A. Onal, G. R. Koirala, T.-I. Kim, S. Nizamoglu, *Chem. Soc. Rev.* **2023**, *52*, 3326.

[16] J. Choi, I. S. Lee, J. S. Lee, S. Jeon, W. S. Yun, S. Yang, Y. Moon, J. Kim, J. Kim, S. Choy, *Biomater. Res.* **2022**, *26*, 56.

[17] J. S. Lee, J. Choi, G. Y. Park, S. J. Kang, J. h. Yang, Y. Lee, M. Choi, K. Kim, T. Kim, *Small* **2023**, *19*, 2300753.

[18] A. Grebinyk, S. Prylutska, O. Chepurna, S. Grebinyk, Y. Prylutskyy, U. Ritter, T. Y. Ohulchanskyy, O. Matyshevska, T. Dandekar, M. Frohme, *Nanomaterials* **2019**, *9*, 1540;

[19] J. Liang, X. Jin, B. Chen, J. Hu, Q. Huang, J. Wan, Z. Hu, B. Wang, *Nanotechnology* **2020**, *31*, 195103;

[20] S. Hameed, P. Bhattarai, X. Liang, N. Zhang, Y. Xu, M. Chen, Z. Dai, *Theranostics* **2018**, *8*, 5501.

[21] a) H. Arami, C. B. Patel, S. J. Madsen, P. J. Dickinson, R. M. Davis, Y. Zeng, B. K. Sturges, K. D. Woolard, F. G. Habte, D. Akin, *ACS Nano* **2019**, *13*, 2858; b) S. Rathi, J. I. Griffith, W. Zhang, W. Zhang, J. H. Oh, S. Talele, J. N. Sarkaria, W. F. Elmquist, *J. Intern. Med.* **2022**, *292*, 3.

[22] R. Ruiz-González, P. Milán, R. Bresolí-Obach, J. C. Stockert, A. Villanueva, M. Cañete, S. Nonell, *Cancers* **2017**, *9*, 18.

[23] a) T.-i. Kim, J. G. McCall, Y. H. Jung, X. Huang, E. R. Siuda, Y. Li, J. Song, Y. M. Song, H. A. Pao, R.-H. Kim, *Science* **2013**, *340*, 211; b) G. Park, H. J. Chung, K. Kim, S. A. Lim, J. Kim, Y. S. Kim, Y. Liu, W. H. Yeo, R. H. Kim, S. S. Kim, *Adv. Healthcare Mater.* **2014**, *3*, 515.

[24] L. Zeng, Y. Pan, R. Zou, J. Zhang, Y. Tian, Z. Teng, S. Wang, W. Ren, X. Xiao, J. Zhang, *Biomaterials* **2016**, *103*, 116.

[25] J. Choi, M. K. Shim, S. Yang, H. S. Hwang, H. Cho, J. Kim, W. S. Yun, Y. Moon, J. Kim, H. Y. Yoon, *ACS Nano* **2021**, *15*, 12086.

[26] E. Donohue, A. Tovey, A. W. Vogl, S. Arns, E. Sternberg, R. N. Young, M. Roberge, *J. Biol. Chem.* **2011**, *286*, 7290.

[27] M. Masquelier, R. Baurain, A. Trouet, *J. Med. Chem.* **1980**, *23*, 1166.

[28] Y. N. Konan-Kouakou, R. Boch, R. Gurny, E. Allemann, *J. Controlled Release* **2005**, *103*, 83.

[29] M. K. Shim, J. Park, H. Y. Yoon, S. Lee, W. Um, J.-H. Kim, S.-W. Kang, J.-W. Seo, S.-W. Hyun, J. H. Park, *J. Controlled Release* **2019**, *294*, 376.

[30] E. T. Papish, *Photochem. Photobiol.* **2023**, *99*, 872.

[31] a) G. Lavie, C. Kaplinsky, A. Toren, I. Aizman, D. Meruelo, Y. Mazur, M. Mandel, *Br. J. Cancer* **1999**, *79*, 423; b) A. P. Castano, P. Mroz, M. R. Hamblin, *Nat. Rev. Cancer* **2006**, *6*, 535.

[32] K. L. Rock, H. Kono, *Annu. Rev. Pathol.: Mech. Dis.* **2008**, *3*, 99.

[33] a) P. Zhang, C. Hu, W. Ran, J. Meng, Q. Yin, Y. Li, *Theranostics* **2016**, *6*, 948; b) M. Swierczewska, R. M. Crist, S. E. McNeil, *Characterization of nanoparticles intended for drug delivery*, Springer, Berlin **2018**, 3; c) M. H. Akhter, J. Ahmad, M. N. Javed, R. Haque, H. Khalilullah, M. Gupta, J. Ali, *Cancer Nanotheranostics* **2021**, *1*, 275.

[34] W. M. Pardridge, *Adv. Drug Delivery Rev.* **1995**, *15*, 5.

[35] M. A. Doustvandi, F. Mohammadnejad, B. Mansoori, H. Tajalli, A. Mohammadi, A. Mokhtarzadeh, E. Baghbani, V. Khaze, K. Hajiasgharzadeh, M. M. Moghaddam, *Photodiagn. Photodyn. Ther.* **2019**, *28*, 88.

[36] a) S. W. Schneider, T. Ludwig, L. Tatenhorst, S. Braune, H. Oberleithner, V. Senner, W. Paulus, *Acta Neuropathol.* **2004**, *107*, 272;

© 2024 The Author(s). Advanced Functional Materials published by Wiley-VCH GmbH

16163028, 2024, 30, Downloaded from https://onlinelibrary.wiley.com/doi/10.1002/adfm.202316386 by Ewha Womans University Library, Wiley Online Library on [10/11/2024]. See the Terms and Conditions (https://onlinelibrary.wiley.com/terms-and-conditions) on Wiley Online Library for rules of use; OA articles are governed by the applicable Creative Commons License

b) K. T. Householder, D. M. DiPerna, E. P. Chung, G. M. Wohlleb, H. D. Dhruv, M. E. Berens, R. W. Sirianni, *Int. J. Pharm.* **2015**, *479*, 374.
[37] Y. Cheng, J. Zou, M. He, X. Hou, H. Wang, J. Xu, Z. Yuan, M. Lan, Y. Yang, X. Chen, *J. Controlled Release* **2024**, *367*, 167.
[38] a) V. Torchilin, *Adv. Drug Delivery Rev.* **2011**, *63*, 131; b) H. Maeda, J. Wu, T. Sawa, Y. Matsumura, K. Hori, *J. Controlled Release* **2000**, *65*, 271.
[39] E. Dunbar, A. T. Yachnis, *Adv Anat Pathol* **2010**, *17*, 187.
[40] a) J. Lipková, B. Menze, B. Wiestler, P. Koumoutsakos, J. S. Lowengrub, *J. R. Soc., Interface* **2022**, *19*, 20210922; b) C. McKinnon, M. Nandhabalan, S. A. Murray, P. Plaha, *BMJ* **2021**, *374*, 1931.
[41] J. S. Lee, S. J. Kang, J. H. Shin, Y. J. Shin, B. Lee, J. M. Koo, T. i. Kim, *Adv. Mater.* **2020**, *32*, 1908422.

© 2024 The Author(s). Advanced Functional Materials published by Wiley-VCH GmbH

16163028, 2024, 30, Downloaded from https://onlinelibrary.wiley.com/doi/10.1002/adfm.202316386 by Ewha Womans University Library, Wiley Online Library on [10/11/2024]. See the Terms and Conditions (https://onlinelibrary.wiley.com/terms-and-conditions) on Wiley Online Library for rules of use; OA articles are governed by the applicable Creative Commons License